Engineering design of the ITER Collective Thomson Scattering diagnostic. Contract EFDA 06-1478

Michelsen, Poul; Furtula, Vedran; Korsholm, Søren Bang; Leipold, Frank; Meo, Fernando; Salewski, Mirko; Bindslev, Henrik; Lauritzen, Bent; Lucas, Matthieu; Nonbøl, Erik

Publication date:
2009

Document Version
Publisher's PDF, also known as Version of record

Engineering design of the ITER Collective Thomson Scattering diagnostic. Contract EFDA 06-1478

Risø-R-Report

P.K. Michelsen, V. Furtula, S.B. Korsholm, F. Leipold, F. Meo, M. Salewski, H. Bindslev, B. Lauritzen, M. Lucas, E. Nonbøl
Risø-R-1717(EN)
December 2009

Risø DTU
National Laboratory for Sustainable Energy

Author: P.K. Michelsen, V. Furtula, S.B. Korsholm, F. Leipold, F. Meo, M. Salewski, H. Bindslev, B. Lauritzen, M. Lucas, E. Nonbøl
Title: Engineering design of the ITER Collective Thomson Scattering diagnostic. Contract EFDA 06-1478
Division: Plasma Physics and Technology Programme

Risø-R-1717(EN)
December 2009

Abstract (max. 2000 char.):

This report describes the work done under EFDA contract 06-1478 (EFDA Ref.: TW6-TPDS-DIASUP10). The main part of the work has been focused on:
1) An outline plan for the full development of the CTS diagnostic for ITER, including specifications for future design tasks on the system and R&D tasks on critical components.
2) An engineering design and test in a blanket mock-up of the front-end quasi-optical High Field Side (HFS) antenna system,.
3) Some considerations on the waveguide mounting.
4) Neutronics and thermo-elastic calculations on nuclear and radiative heating of the first mirror required to provide input to the engineering design.
5) An engineering design of the front-end quasi-optical components for the Low Field Side (LFS) system in the port plug.
6) A discussion on possible calibration methods.

ISSN 0106-2840
ISBN 978-87-550-3793-9

Contract no.:
EFDA 06-1478

Group's own reg. no.:
1710019-26

Sponsorship:
European Commission and EFDA

Cover :

Pages: 45
Tables: 5
References: 15

Information Service Department
Risø National Laboratory for Sustainable Energy
Technical University of Denmark
P.O.Box 49
DK-4000 Roskilde
Denmark
Telephone +45 46774005
bibl@risoe.dtu.dk
Fax +45 46774013
www.risoe.dtu.dk

Contents

Preface **4**

1 Outline plan **5**

1.1 Overview of the outline plan 5
1.1.1 Outline plan for the ITER LFS CTS diagnostic 5
1.1.2 Outline plan for the ITER HFS CTS diagnostic 7
1.2 Key R&D tasks on critical components 9

2 Engineering design of the front-end quasi-optical components for the HFS antenna system **10**

2.1 Summary 10
2.2 Calculation of the HFS beam 10
2.3 Horn 12
2.4 The HFS receiver 14
2.5 Blanket module 17
2.6 Waveguides for ITER HFS receiver 19
2.7 Neutronics and Thermo-Elastic Modelling of the First Mirror of the HFS CTS system 20
2.7.1 Summary 20
2.7.2 Neutronics Modelling 21
2.7.3 Thermo-Elastic Modelling 23
2.7.4 Plasma Steady-State Power Balance 23
2.7.5 Mirror Steady-State Power Balance 24
2.7.7 Numerical Methods 25
2.7.8 Uncertainties and Limitations 26
2.7.9 Mirror Geometries 26
2.7.10 Maximum Temperatures 28
2.7.11 Maximum Displacements 30
2.7.12 Maximum von Mises Stresses 31
2.7.13 Massive versus Hollow Support Arm 32
2.7.14 Conclusions 33

3 Waveguide mounting on the inner vacuum wall **34**

3.1 HFS waveguides feed-through the upper port duct 34

4 Design study of the window assemblies **35**

5 Engineering design of the front-end quasi-optical components for the LFS system **36**

5.1 The LFS launcher beam 36
5.2 The LFS receiver 37
5.2.1 Two mirror solution 37
5.2.2 One mirror solution 39

6 Calibration methods **40**

7 Documentation **42**

8 IPR **42**

Preface

The EFDA contract 06-1478 (EFDA Ref.: TW6-TPDS-DIASUP10) with Association EURATOM Risø DTU under the task title: Support of diagnostic design for ITER concerns an engineering design of the ITER Collective Thomson Scattering diagnostic. In the technical specifications the following introduction is presented:

A feasibility study and conceptual design of the collective Thomson scattering (CTS) diagnostic has been performed and detailed design initiated [1]-[3]. Various R&D issues critical to the viability of the CTS diagnostic on ITER have been identified and the most urgent ones, which deal with optimization of mirrors and horns at the High Field Side (HFS) antenna system, are being addressed by experiment and numerical modelling [4]. On the basis of the previous design analysis and the optimization, engineering designs should be developed for both the HFS receiver system (both antenna and waveguides) and of the port-mounted components, by addressing the critical issues (such as limited space, nuclear heating and neutron streaming). It is important to demonstrate the technical feasibility of the diagnostics, and to document the value of the various subsystems and impact of constraints (such as whether or not blanket-module cut-outs are accepted for this diagnostic) before decisions can be taken on the inclusion of the CTS diagnostic in the ITER diagnostic procurement packages. Due to the many machine interfaces, integration of the in-vessel components of the HFS receiver system is most urgent, whereas it may only be possible to advance the integration of the LFS CTS-diagnostic components in the port plug at a conceptual level, given the interfaces with other diagnostics in the same port. Depending on the status of formal inclusion of the CTS diagnostic in the ITER diagnostic procurement packages and on whether during the execution of this contract the formal responsibility for diagnostic integration in the relevant equatorial port plug (foreseen to be equatorial port 12) is transferred from the ITER IT to the party supplying the equatorial port plug, it may be possible to start design iterations to establish the boundary conditions on the integration of the diagnostic in the port plug.

The work is described in the following chapters where the first paragraph of each section (in italic) describes the requested contribution.

1 Outline plan

Propose a comprehensive outline plan for the full development of the CTS diagnostic for ITER, including detailed specifications for future design tasks on the system and R&D tasks on critical components.

The present report provides a number of important steps towards a design of the ITER CTS diagnostic. However, the route towards the full realisation of the CTS diagnostic system at ITER comprises several further steps. This chapter comprises a proposal for a comprehensive outline plan towards the full development. After the presentation of the outline plan, an overview of key R&D tasks on critical components is presented.

1.1 Overview of the outline plan

For practical reasons the outline plan is divided in two – one covering the LFS (perpendicularly viewing) part, the other covering the HFS (parallel viewing) part of the diagnostic system. The basis of the plan is the preceding and the current task.

1.1.1 Outline plan for the ITER LFS CTS diagnostic

1. Determination of the optimal antenna mirror configuration.

   Gaussian beam calculations, supported by modeling of the neutron and heat load on the mirror antenna should be extended in order to choose the optimal configuration (1-mirror or 2-mirror), while also taking into account integration issues.

2. Design of mirrors

   Presently the mirror surfaces have been modeled and designed; however, it is a significant task to determine the right material for and thickness of the bulk of the mirror, while also sufficient and efficient cooling should be designed – taking into account the available cooling in the port plug. Some experience from existing mirror designs will be taken into account.

3. Design of waveguide path

   The optimal path of the low power receiver waveguides and the high power gyrotron waveguides must be found, while taking into account minimization of losses and neutron streaming. The paths should fit into the expected modules of the port plug, and also fit in with the other equipment and viewing lines in the port plug (see also point 7).

4. Design of the gyrotron transmission line

   The gyrotron transmission line includes two mirrors, which are handled under point 2 above. The determination of the optimal path of the transmission line is described above (see point 3), however the gyrotron transmission line has an additional challenge, since the fundamental resonance of the 60 GHz radiation is crossed in the equatorial port plug. Previously, similar challenges have been

seen on FTU, and solutions have been proposed. Both calculations and mockup experiments (possibly on FTU) is needed.

5. Design of mountings for mirrors and waveguides

   The design of the mounting of the mirrors and the waveguides are important, due to e.g. heat conduction, stability, and integration. It is expected that solutions to this to a large extent can be drawn from other similar equipment, however, some of the mirrors are larger and more exposed than any other equipment in ITER.

6. Mirror heat load calculations and optimization of mirror design (iterative)

   Modeling of heat load (due to neutrons and gammas) has already been performed. This modeling needs to be extended and any new design of bulk mirrors (3D – not just surfaces) should be tested with this modeling in order to optimize the size, the shape, the edges, the cooling etc. Obviously, this process will be iterative with several of the points above.

7. Resolving integration issues in equatorial port plug 12 (iterative)

   Work has already been performed towards resolving the integration issues in the equatorial port plug #12. Some guidelines for the required space and possible solutions have been agreed between Risø DTU, ITER, and the Chinese port plug engineer. This work will be a continual and iterative process as the final design is approached.

8. Design of feedthroughs and windows

   Feedthroughs for the waveguides crossing the vacuum boundary and the bioshield must be designed. The size of these will be a compromise between space and transmission losses. Windows – possibly in-waveguide windows – are essential components, but solutions for the low power receiver transmission lines may be found in collaboration with e.g. the reflectometry diagnostics. A window that can withstand the high power of the gyrotron transmission line is a challenge, and since the heating gyrotrons of ITER operates at a different frequency, some development may be needed. A commercial partner has already offered assistance on this task.

9. Tentative final engineering design

   Having solved the tasks in the above points, a tentative version of the final engineering design can be made. This design will form the basis of the neutronics analysis in the next point, and if successful will be the design for the mockup.

10. Neutronics and thermal stress calculations of the full CTS system and surroundings

    It is crucial that the full CTS system, including the modifications of the surrounding structures passes the analysis of the neutron irradiation. Additionally, the accompanying thermal stress (which also is affected by the gammas etc.) modeling should be performed.

11. Mockup of all CTS related structures in the equatorial port plug #12

In order to verify the design, identify unforeseen challenges, and optimize the solutions, a full 1:1 mockup of the CTS related structures in port plug #12 should be constructed.

12. Final detailed engineering design

    Based on the above points the final detailed engineering design can be established. This may form the basis for the procurement actions, provided all involved parties agrees on the design solution.

13. ITER approval of design

    A mandatory step towards the installation of the ITER CTS diagnostic is naturally that the ITER organization and Fusion for Energy approves the final detailed engineering design.

14. Specification and procurement of gyrotron

    At a later stage the specification and procurement of the gyrotron will be initiated. It is not expected that this will pose a significant problem, but some development of a 60 GHz 1 MW gyrotron will be needed. In short: 60 GHz gyrotrons exist, as also 1 MW gyrotrons at higher frequencies. As the power should be easier to achieve at a lower frequency, the task should be achievable.

15. Specification of receiver electronics and data acquisition hardware

    The receiver consists of an RF part in the 60 GHz range, which enters a mixing stage bringing the received signal to an intermediate frequency (IF). This IF part of the receiver then enters data acquisition cards. The RF part of the receiver can readily be designed, and in the 60 GHz range standard solutions would be available from manufacturers; however, the architecture of the CTS receiver IF electronics will not be decided until a few years before use. This is due to the rapid development of electronics, ADC's, computers etc. It may well be possible that sufficient resolution and sampling rate can be provided, so that only a number of mixing stages will be needed in the IF part entering super fast data acquisition cards making digital filtering possible.

    However, a component that will be needed in any case in the RF part is the notch filter, which will block stray light from the gyrotron. It is a feasible R&D task to produce such a notch filter, but it will require substantial R&D to develop and optimize the component.

16. Creation of receiver mockup

    In due time, a full test receiver should be constructed to identify possible shortcomings before 10 identical receivers are procured.

17. Procurement of receivers

1.1.2 Outline plan for the ITER HFS CTS diagnostic

Several of the steps for the development of the HFS CTS diagnostic are similar to the steps for the LFS development described above. For completeness all steps are mentioned for the HFS, but in the case of repetition of the points above, no detailed explanations are given, and the reader is referred to the explanations in the outline plan for the LFS CTS diagnostic.

1. Optimise the antenna mirror configuration.

The design and tests of a 4-mirror HFS antenna solution is presented in this report. The design and the tests should become more complete, in order to determine the optimal design of the antenna. The location of the receiver horns in relation to the mirrors and the waveguides are crucial for the receiver beam pattern and the resolution of the diagnostic.

2. Design of mirrors
3. Design of waveguide path

   The path of the HFS waveguides is particularly challenging, since it follows the vacuum vessel wall behind the blanket modules. However, this is also the case for e.g. the HFS reflectometry. The optimized path should take into account that the losses of the long transmission line should be minimized.

4. Design of the gyrotron transmission line
5. Design of mountings for mirrors and waveguides

   Mountings of both the mirrors and the waveguides are more challenging on the HFS, where attention needs to be paid to the requirements of electrical isolation.

6. Mirror heat load calculations and optimization of mirror design (iterative)
7. Resolving integration issues in equatorial and upper port plug 12.

   Since the gyrotron transmission line for the HFS system also enters through equatorial port plug #12, similar integration issues as for the LFS have to be resolved. Furthermore, there are also integration issues in the upper port plug #12, where the waveguide from the HFS is exiting the vessel. A preliminary look at this issue is being presented in this report, but more work is needed to come to a final solution of the integration issues and the design of the waveguide feedthroughs.

8. Design of feedthroughs and windows

   The task is similar to the LFS task in point 8 above, but it should be mentioned that for the HFS waveguides the space provided for exiting the upper port plug #12 may be restricted, and innovative solutions may be needed.

9. Tentative final engineering design
10. Neutronics and thermal stress calculations of the full CTS system and surroundings

    Again, this point is like the point 10 for the LFS above, but it should be mentioned that the neutronic irradiation effect of the cut-outs of the HFS blanket should be carefully examined and verified.

11. Mockup of all CTS related structures on the HFS inner wall and upper port #12
12. Final detailed engineering design
13. ITER approval of design
14. Specification and procurement of gyrotron
15. Specification of receiver electronics and DAQ
16. Creation of receiver mockup

17. Procurement of receivers

1.2 Key R&D tasks on critical components

The steps described above are naturally all important in order to arrive at the desired goal of an ITER CTS diagnostic. Among the listed tasks some critical components need special attention. These include:

1. Design of mirrors.

   As described above the bulk of the mirrors should be carefully designed, paying attention to material, thickness, shape, cooling, etc. Some inspiration from other diagnostics will be included, but the large sizes of some of the mirrors have not been seen in the ITER designs before. Therefore, particular solutions may be required. It is foreseen that a number of mirror mockups needs to be constructed in order to test capabilities, like thermal conduction, cooling, and mechanical stability.

2. Design of in-vessel horns

   The shape of the in-vessel horns on both the LFS and HFS are crucial for the interaction with the mirrors and hereby the beam patterns in the plasma. A number of different horns need to be designed and produced in order to gain experience with tailoring the horns and hence the beam shapes.

3. High power transmission lines for probing gyrotron radiation

   Transmission of 1 MW of gyrotron power over a length of several tenths of meters of waveguide is a task that has been done in the past. However, a challenge for the ITER CTS system is the crossing of the fundamental resonance. Previously, similar challenges have been seen on FTU, and solutions have been proposed. Both calculations and mockup experiments (possibly on FTU) are needed, in order to approach a technical solution for the ITER CTS diagnostic.

4. Development of high power vacuum window

   As mentioned above, a window that can withstand the high power in the gyrotron transmission line is a challenge, and since the heating gyrotrons of ITER operate at a different frequency, some development may be needed, since vacuum windows at high power needs to be tailored to the right frequency. A commercial partner has already offered assistance on this task, and while it needs special attention, it should be a surmountable task.

5. Development of 60 GHz notch filters for the CTS receivers

   The development of highly efficient notch filters is being done in a few places in the world; particularly in the USA. In order to be more independent of suppliers, and be capable of optimizing the essential notch filters, an effort should be put into developing the notch filters for the ITER CTS receivers.

The list should not be regarded as exhaustive, since new key R&D tasks would be expected to emerge during the development.

2 Engineering design of the front-end quasi-optical components for the HFS antenna system

Perform an engineering design of the front-end quasi-optical components for the HFS antenna system, including all necessary mirrors and receiver horns and their mounting on the inside vessel surface. Thermo-mechanical calculations will be required on nuclear and radioactive heating to provide input to the engineering design (on the effect of heating of components, adequate choice of materials, cooling provisions, possible size, thermal expansion and mounting). The design should consider the allowable and required cut-outs in blanket modules (both for adequate microwave-beam transmission and space for mirrors and horns), including assessments of the performance if limitations on cut-outs were imposed.

2.1 Summary

The plasma is viewed via a slot between the blanket modules. The horizontal dimension is defined by the multiple beams required for different spatial CTS measurements. The vertical dimension is a compromise between CTS signal strength and limiting neutron flux/fluence to the inner coils. The present size is 350 x 30 mm
The HFS receiver system consists of a mirror assembly and a receiver horn antenna consisting of 10 individual horns. The slot poses a problem of a highly astigmatic beam. In order to avoid mirrors with high curvature, a four mirror module has been designed that lengthen the overall optical path. The module is embedded behind the blanket module is used to couple beams from this slot to a near circular horn array. The four mirror assembly transforms the astigmatic anisotropic Gaussian beam (approximate size: 100 mm x 10 mm) coming from the slot to an isotropic Gaussian beam with a beam waist of 4.5 mm corresponding to a divergence angle of 20.3˚, which is accepted by an antenna horn. In order to verify the proper operation of the receiver system, which was modelled in Matlab and designed in CATIA, a 1:1 mock-up has been built; initially only with one antenna horn. The mock-up consists of the HFS receiver antenna module and relevant parts of the involved blanket modules. The verification of the beam propagation is accomplished by feeding the antenna horn with mm-waves from a Gunn diode (60 GHz) and tracking the beam shape backwards. The beam is guided through the quasi-optical transmission line and detected by a detector diode mounted on a two-dimensional translation stage.

2.2 Calculation of the HFS beam

For the CTS HFS receiver antenna, a horizontal slot of approximately 350 x 30 mm in the blanket should be available in order to satisfy the measurements requirement for the confined alphas. A beam with a high astigmatism travelling through the slot needs to be converted to a small symmetrical beam with small ellipticity suitable for a symmetrical horn antenna. Avoiding mirrors with excessive curvature requires a long travel path for beams with large spatial extension, which shall be focused to a

small horn. This is the case for the horizontal extension of the beam (Gaussian radius: 100 mm at the slot). Since the vertical extension of the beam (9.4 mm) is smaller than the horizontal one, the beam would diverge most in the vertical direction along the travel path. This challenge of focusing a high astigmatic beam onto the near circular horn can be overcome by using a 4-mirror transmission line. The resulting long travel path allows the horizontal extension to be focused to a radius of 4.5 mm, while the 2 additional mirrors allow refocusing the beam in the vertical plane. The beam propagation was calculated in Matlab. In order to include more than 99% of the beam power, the effective opening size of the antenna should be at least 1.6 times the Gaussian width. (A Gaussian beam with the radii 100 and 9.4 mm requires a slot of 320mm x 30 mm)
Figure 1 shows the beam radii in the vertical and horizontal direction versus the travel path after it passes the slot in the blanket. The green circles in the graph indicate the position of the mirrors. The blue circle is the position of the horn antenna. Figure 2 shows the calculated beam path.

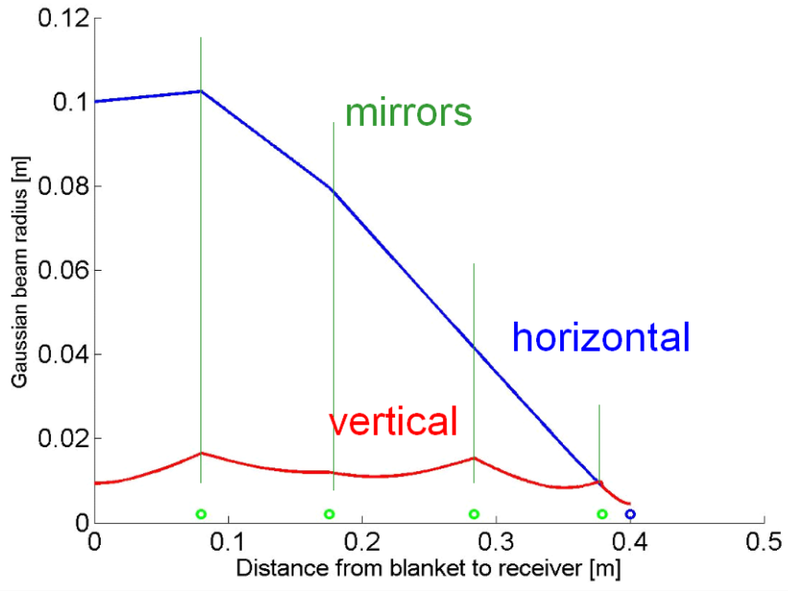

Figure 1: beam radii in the vertical and horizontal direction versus the travel path after it passed the slot in the blanket. The green circles in the graph indicate the position of the mirrors. The blue circle is the position of the horn antenna.

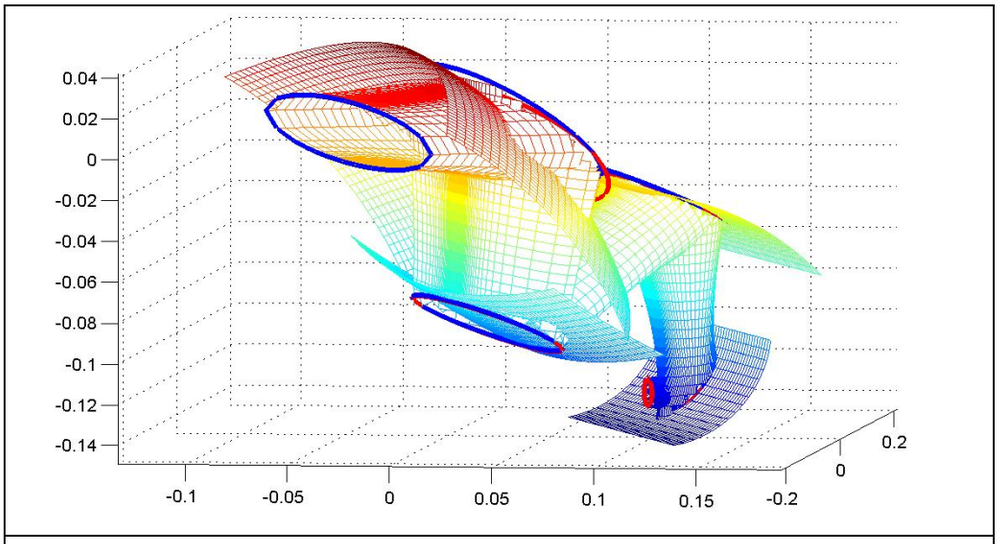

Figure 2: Beam path through the four mirror antenna as calculated in Matlab.

2.3 Horn

The beam characteristic at the receiver end was calculated in 2.2. According to the calculations, the horn shall be capable of receiving an isotropic beam with a waist radius of 4.5 mm corresponding to a divergence angle of 20.3˚. Based on [5], a corrugated horn antenna for a frequency of 60 GHz was designed and built (Figure 3). Figure 4 shows a picture of the horn.

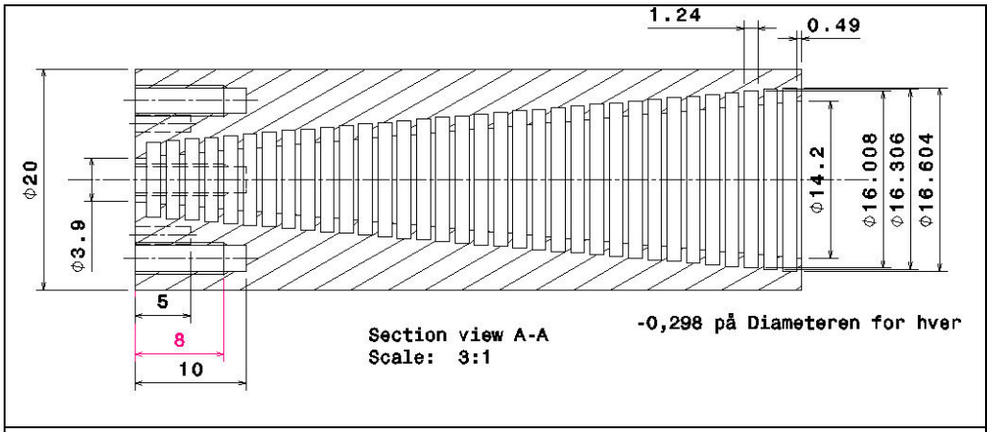

Figure 3: Design drawing of the corrugated antenna horn for 60 GHz. The overall length of the horn is 60 mm. The left side shows the interface to a circular fundamental waveguide.

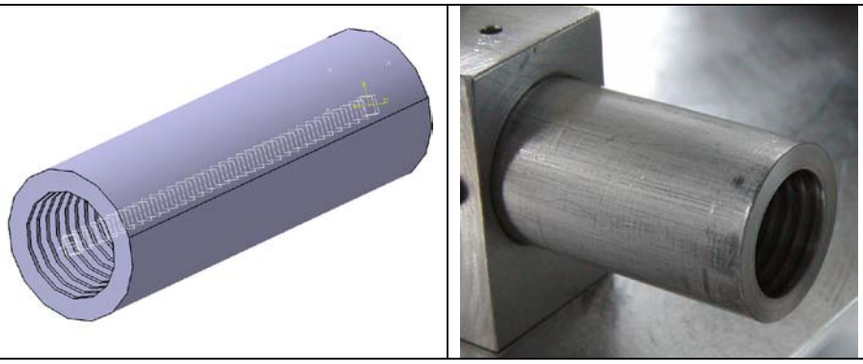

Figure 4 Circularly corrugated horn antenna for 60 GHz (left: CATIA drawing; right: photo)

In order to verify whether the horn meets the requirements, a 60 GHz Gunn diode was mounted at the port of the horn and the device was used as a mm-wave source. The beam pattern in front of the horn opening was measured at various distances from the horn using a detector diode mounted on a translation stage and moving and measuring in two dimensions perpendicular to the beam propagation (Figure 5). The results of the measurements are shown in Table 1. W1 and W2 is the beam radius in two orthogonal directions (major and minor axes of the generally elliptical beam shape). Figure 6 shows the beam radius versus the distance from the horn for major and minor axis. From these measurements, the divergence angles are obtained. They were found to be 19˚ and 19.8˚ for the major and minor axis, respectively. Figure 6 shows also the theoretical expected beam waist versus distance. The measurements are in good agreement with the expected specification. The beam waists can be calculated from the divergence angles and are found to be 4.8 mm and 4.6 mm, respectively.

Distance from horn [mm]	W_1 [mm]	W_2 [mm]
194	72.6	75.6
245	89.3	92.5
320	113.5	115.9
415	145.4	147.9
500	174.0	180.7

Table 1: Measurements of the beam radius for various distances from the horn.

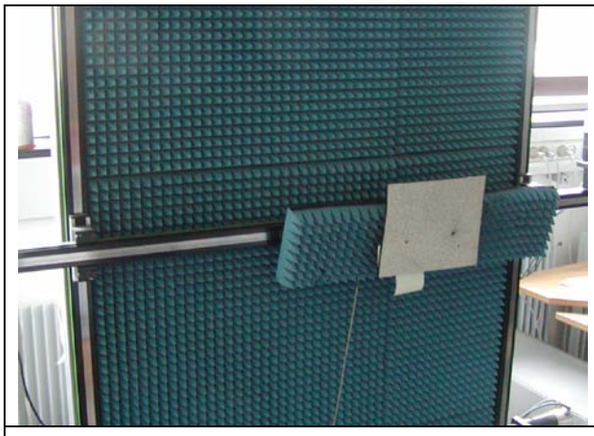

Figure 5: Detector diode mounted on a translation stage and moving in two dimensions.

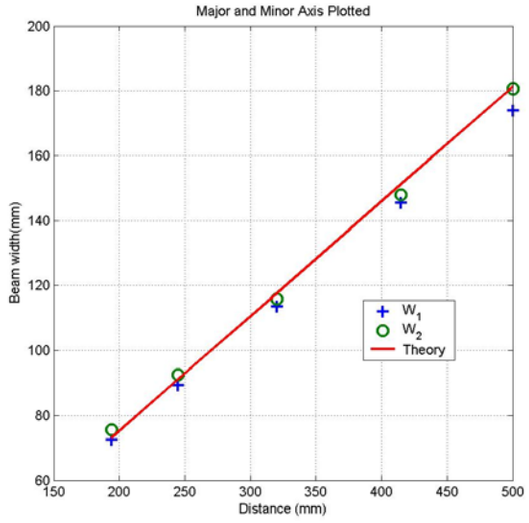

Figure 6: Envelope of the beam leaving the horn. W1 and W2 should be identical, as the horn has a circular symmetry. The difference is less than 3% between the measured beams in two orthogonal directions.

It was only possible to verify the divergence angle within a distance of 0.5 m from the horn. For longer distances the beam width was too large resulting in a low signal and consequently in a low S/N ratio.

2.4 The HFS receiver

A schematic of the mirror assembly and the horn is shown in Figure 7. Figure 8 shows a 3D picture of the quasi-optical receiver antenna.

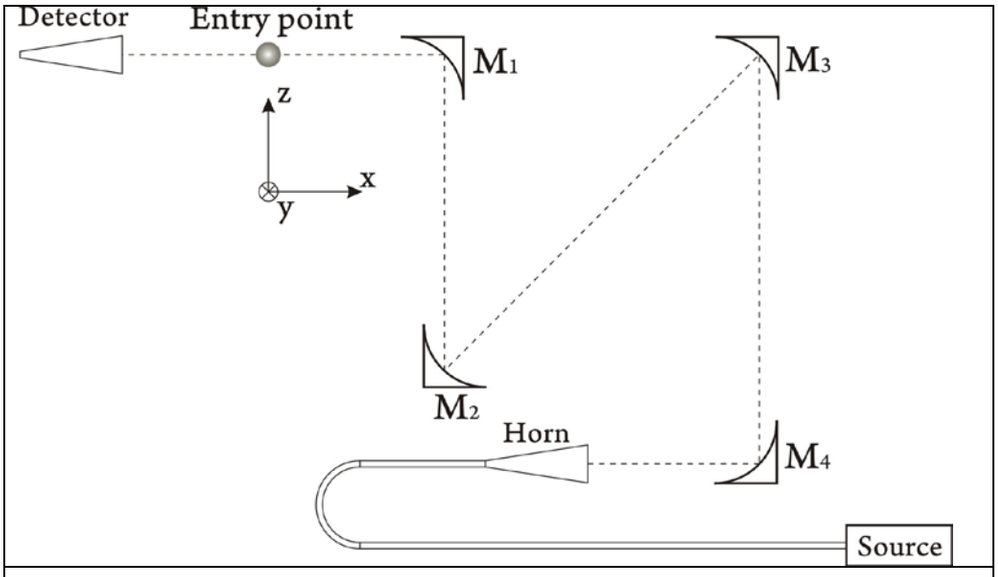

Figure 7: Schematic of receiver system and detector. The detector is movable in the y-z-direction. Mirror M1 is the plasma facing mirror.

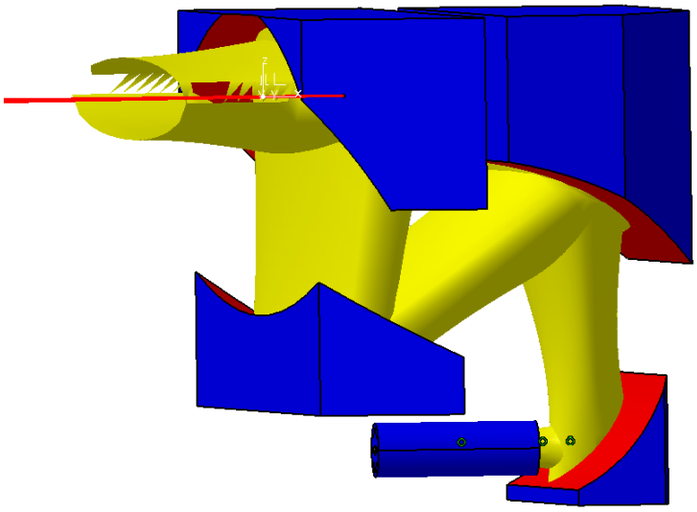

Figure 8: 3D picture from CATIA of the HFS receiver antenna.

In order to verify the beam geometry calculated in 2.2, a 1:1 mock-up of the mirror system is built. The mirror assembly is manufactured in aluminium for cost and ease of machining. Figure 9 shows photographs of the mirror assembly.

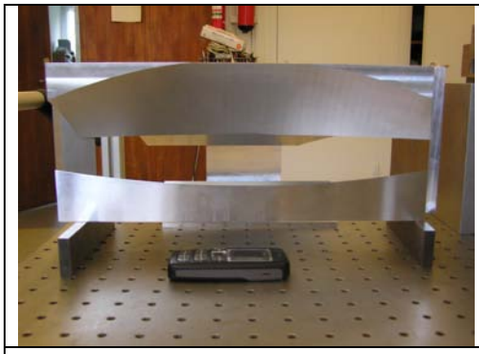

Figure 9: a: Mirror assembly (front view)

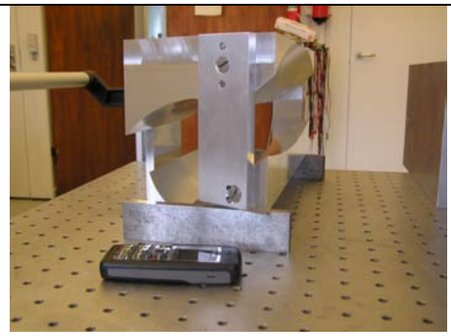

b: Mirror assembly (side view)

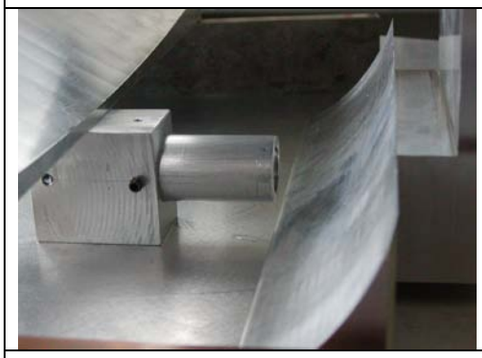

c: Horn antenna facing the last mirror

In order to test the mirror assembly, the horn antenna is integrated into the mirror assembly (see Figure 8). A detector, which is movable in the y-z-plane is used to characterize the beam pattern at various distances x from the mirror M1. The beam widths in two orthogonal directions at various distances from mirror M1 are shown in Table 2 and **Error! Reference source not found.**. The beam passes the quasi-optical transmission line in the reverse direction. Ideally, W1 is the beam size in the z-direction (vertical) and W2 is the beam size in the y-direction (horizontal). However, the major and minor axes of the elliptical beam pattern deviate slightly from the y- and z-axis, respectively.

The left graph in Figure 10 shows the divergence of the beam at M1 in the vertical direction. The beam waist is calculated from the divergence angle and is found to be 9.49 mm. This is in good agreement with the calculated value of 10 mm. The right graph in Figure 10 shows convergence of the beam at M1 in the horizontal direction. The divergence angle is difficult to obtain, because an extrapolation to a distance of 3.5 m (theoretical beam waist) is subject to large errors.

D[mm]	W_1[mm]	W_2[mm]
123	15.2	100.7
172	24.1	92.9
214	31	93.3
260	36.2	86.7
348	51.6	84.6

Table 2: The measured points given by the diode detector are fitted to a Gaussian beam. From the values it is clear that we have an astigmatic beam propagating between the first mirror M1 and the detector.

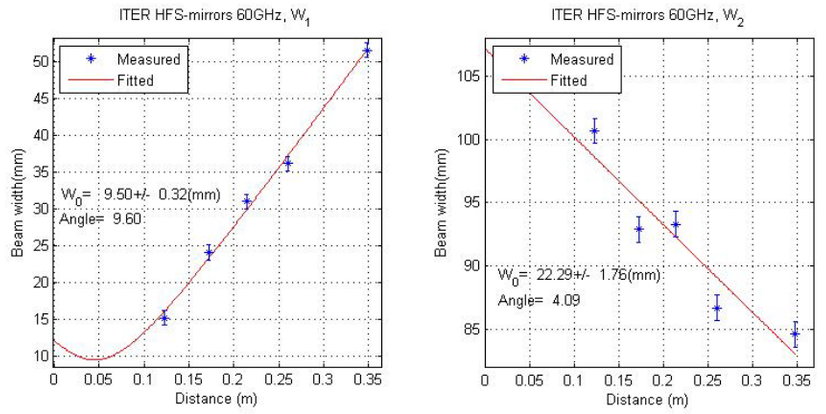

Figure 10: The beam radius at various distances. Left: W1 being the vertical beam width, Right:W2 being the horizontal beam width.

The measured beam expansion in the vertical direction (Figure 10left) and the fitting to a Gaussian beam shape resulting in a beam waist of w_0= 9.49 mm is in good agreement with the theoretical beam waist of 9.375 mm. The measured beam expansion in the y-direction is more difficult. The beam waist in the y-direction is expected to be approximately 2.8 m from the entry point. At this position, the beam intensity is decreased significantly due to the increased beam size and hence low power density resulting in a low S/N ratio for the detector diode. Therefore, the beam could only be measured up to a distance of 0.35 m. The extrapolation to a location 10 times farther away than the range of the measurement is subject to a large error. It can only be concluded from these measurements that the measured beam size in the y-direction (0.103 m at a distance of 50 mm) is in good agreement with the expected size of 0.1 m.

2.5 Blanket module

The proper operation of the mirror system with the horn antenna has been demonstrated. At ITER, the mirror system will be placed behind the blanket, in which a pocket has to be cut out. The side of the blanket facing the plasma has a slit opening of 30 mm x 500 mm through which the scattered beam has to be captured.
The width of the slit opening has been chosen to be 1.6 times the Gaussian width of the captured beam. This will ensure that 99.4% of the light can be fed through the slit. Changes of the slit in the horizontal position due to manufacturing and installation tolerances of the blanket module do not change the horizontal dimension of the beam significantly. Changes in the vertical direction will truncate the beam to 20 mm in the worst case. This is when the upper and lower blanket modules make contact and the gap in between disappears. The remaining gap has still the size of the Gaussian width of the beam in the vertical direction. However, the intensity is reduced to 86%.
In order to test the antenna system with the metal boundary of the blanket, a part of the blanket including the required cut-outs has been made of aluminium. A CATIA drawing of the blanket is shown in Figure 11a. The green surfaces represent the cutting surfaces of the blanket module. A photograph of the 1:1 mock-up is shown in Figure 11b shows the CATIA drawing of the blanket module. The space for the mirrors behind the blanket is limited to 190 mm vertically, 300 mm horizontally, and 230 mm radially.

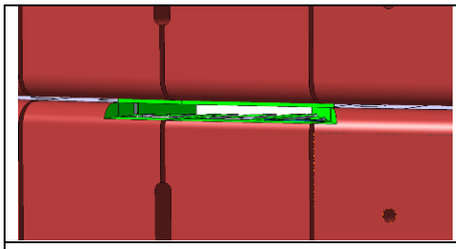

Figure 11a: Blanket design (CATIA)

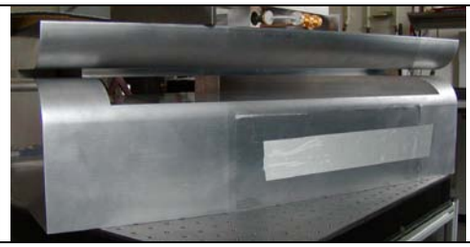

b: Blanket mock-up (1:1)

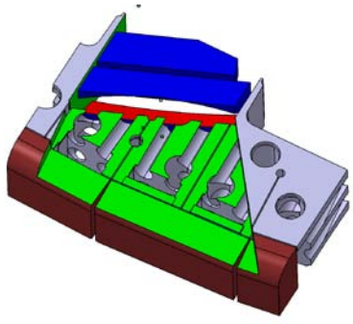

c: Mirror system integrated in the blanket. The mirror system is depicted in blue.

The receiver antenna is integrated in the blanket module to verify the capability of detecting a scattered beam through the slit in the blanket. Measurements of the beam propagation from the slit were performed like the ones performed for the mirror system without the blanket. Results are shown in Figure 12. From the figure it is estimated that the divergence angle of the beam in vertical direction is around 8 degrees. This is slightly more than the 7 degrees calculated in the feasibility study (Ref.:[1]). This will slightly affect the conclusions of this work essentially. We can conclude that a smaller vertical slit opening (hence larger divergence angle) will not be able to satisfy the measurement requirements for the confined alphas unless we increase the gyrotron probing power or increase the integration time and hence lower the time resolution.
The side lobes observed in the lower graphs of Figure 12 are believed to be due to a few imperfections in the blanket module, and can probably be improved. However the total power in the side lobes seems are marginal, and they will therefore only affect the power in the main lobe by a neglectable amount.

This study was only done for the central beam; hence the off-axis beam needs to be studied in the future in order to understand the full performance of the system.

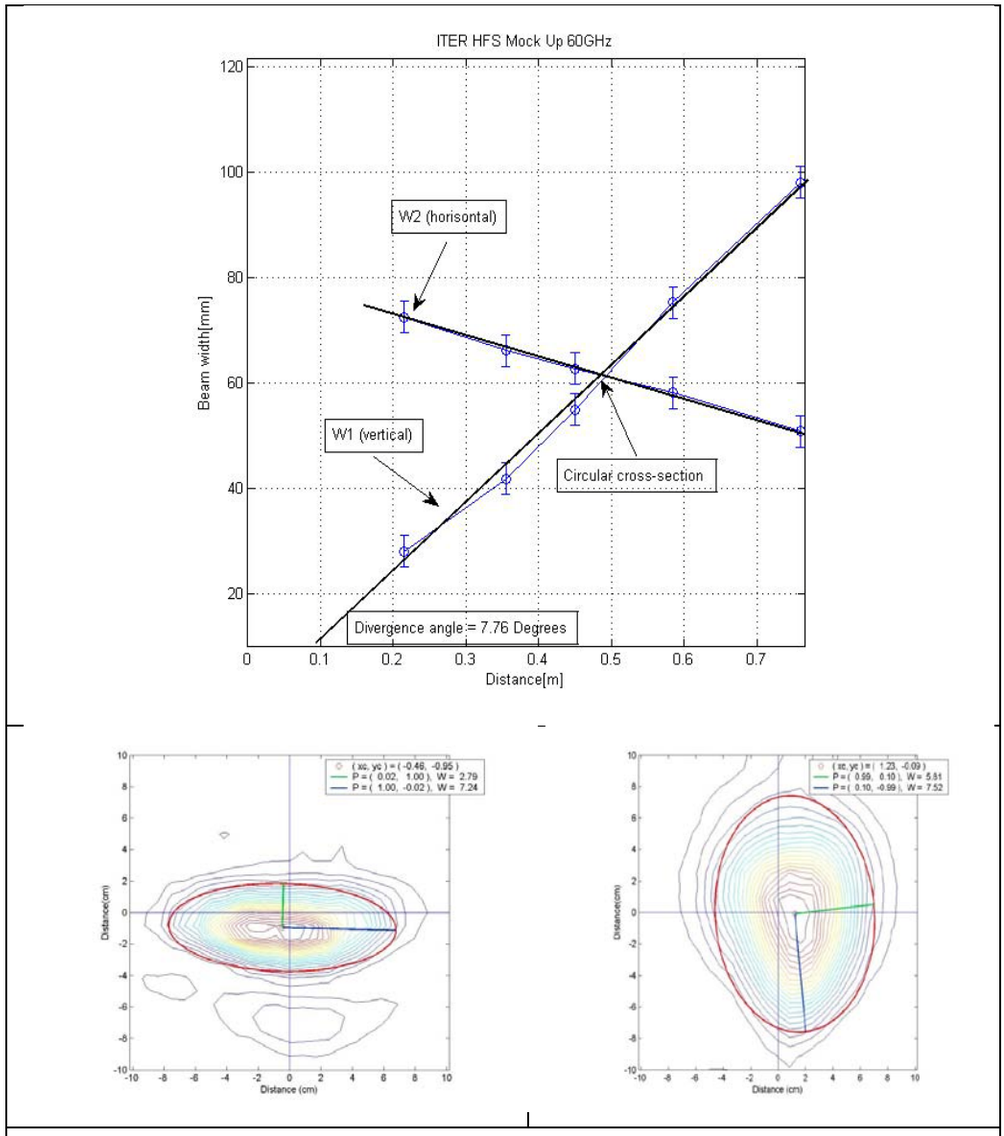

Figure 12:Beam propagation from the ITER blanket model slit. Upper graph: Beam width vs. distance from slit opening. Lower left: Beam cross section at distance 0.215 m. Lower right: Beam cross section at distance 0.585 m.

2.6 Waveguides for ITER HFS receiver

Due to limited space in the blanket module, fundamental waveguides with bends having a curvature radius of several times the wavelength cannot be used, and sharper bends are required. The application of mitre bends is investigated by simulations of the wave propagation by ANSYS. The dimension of the mitre bend is 3.76 x 1.88 mm, which corresponds to a waveguide WR15. The frequency is 60 GHz. The waveguide is excited by a 60GHz wave in mode TE10. The size of the cut off corner was varied to minimize reflection. The S11 parameter was found to be 0.035 corresponding to a power reflection of -29 dB. The simulations demonstrate that mitre bends are suitable for a fundamental waveguide. Figure 13 shows the

electrical field component in y-direction and the energy flux density (pointing vector) through a piece of waveguide containing a mitre bend.

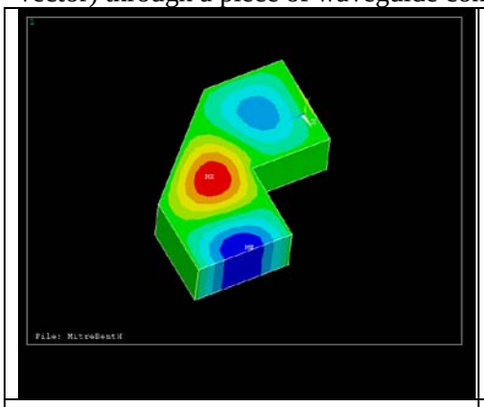

Figure 13 a: strength of the electrical field component perpendicular to the top surface

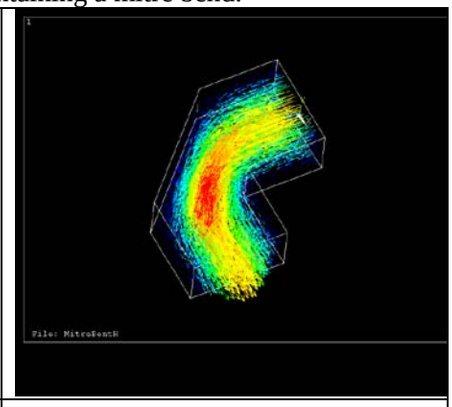

b: Energy flux density (pointing vector) through a mitre bend

2.7 Neutronics and Thermo-Elastic Modelling of the First Mirror of the HFS CTS system

2.7.1 Summary

The first mirror of the high field side (HFS) collective Thomson scattering (CTS) system has a direct line of sight to the plasma and is exposed to severe neutron and photon fluxes. These are further enhanced by the necessity to cut out shielding blanket material due to space limitations on the inboard side (HFS) of the tokamak: There is not enough room to place the receiver behind a blanket of nominal thickness. These thermal loads result in strains in the mirror. The present modelling of neutronics and thermo-elastic stresses indicates that the mirror curvature may warp. This may alter the beam quality, and therefore thermal effects have to be accounted for in the design of the mirror. Various mirror designs are being compared in terms of temperature distribution, the displacement, and thermal strain (after the von Mises failure hypothesis).

The modelling of neutron and γ fluxes is being performed by Monte Carlo simulations with the MCNP-5 code [6] assuming a plasma with 500 MW fusion power. In addition to neutrons, radiation from the plasma mostly in the VUV, UV, and x-ray ranges hits the first mirror. Various cooling systems are considered, as for example passive cooling, drilled internal channels or cooling channels which are welded on the back, optionally facilitated by cooling channels in the mirror. The mirror is assumed to be supported on the back side, allowing for free thermal expansion. The mirror material is assumed to be stainless steel.

There are several main conclusions of the present study. A guiding principle for designing CTS first mirrors is the need to minimize the use of material. Firstly, the mirrors should be thin (~10 mm) to avoid large thermal stresses. Thick mirrors were previously considered to reduce the neutron streaming through the weakened shielding due to the required additional cut-outs. However, the function of absorbing neutrons to protect the superconducting magnets should preferably be separated from the function of

reflecting radiation for diagnostic purposes. The enhanced neutron streaming behind the mirror could be counteracted by a separate neutron absorber if necessary. The lower bound on the mirror thickness is given by thermal footprints of backside features for excessively thin mirrors and by the difficulty to manufacture large mirrors with the given reflecting surfaces. Secondly, the mirror geometry should preferably resemble the beam shape from a thermo-mechanical point of view. As the beam pattern is elliptical in shape, the mirror will as well be as close to elliptical shape as possible (though there are constraints). For example, the corners can be rounded. Though mirrors with corners are easier to manufacture, the material in the corners serves no function and unnecessarily adds to the cooling demand. Thirdly, another example is the support arm of the mirror for which it was found that a hollow holder is advantageous since bending resistance is mostly offered by the outer radii of the holder (with larger second moments of area) whereas the entire holder is approximately uniformly heated by volumetric heating. Material at the centre has therefore less bending resistance per unit heating power and should be avoided, and hollow holders are therefore beneficial. Lastly, it was further shown that it may be necessary to apply active cooling to maintain thermal stresses at an acceptable level and that at key positions sharp edges have to avoided due to thermal stress reduction.

Future work will include a detailed material selection with comparisons of various materials. The material has large impacts on temperature (e.g. via emissivities) and mirror displacement and is a high priority. Various cooling system options will be considered. Additional work will be dedicated to modelling of the reflection of millimetre waves from the thermally deformed mirror as the beam quality may deteriorate. Lastly, design improvements are foreseen for stress reduction purposes.

2.7.2 Neutronics Modelling

The mirrors are subject to heating due to neutron fluxes. The neutrons are generated at 14 MeV from the D-T-process in the fusion plasma. The γ's are generated locally from (n,γ) processes. In the (n,γ) process, a neutron is absorbed giving off its binding energy of 8 MeV to the photon. These neutron and photon fluxes have been calculated in a full 3D Monte-Carlo simulation with the MCNP-5 code [6]. The geometrical model is a simplified version of the ITER-FEAT model which is used for full 3D neutronics calculations for ITER systems. ITER-FEAT has rotation symmetry after 20º to reduce the computational load. This had to be extended to 40º for the detailed simulations since the position of the first mirror does not comply with 20º symmetry. The 40º model is shown in cuts in XZ and XY direction in the left and right of Figure 14, respectively.

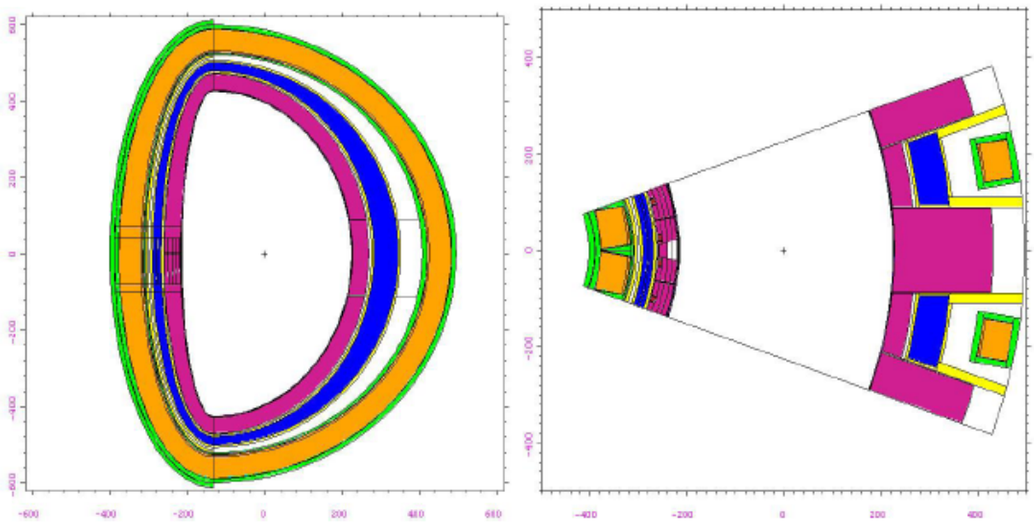

Figure 14 XZ (left) and XY (right) cuts of the 40º model of the torus for neutronic modelling

The CTS HFS system requires a wider optical access to the plasma than it is given by unmodified blanket modules as was shown in 2D electromagnetic wave simulations. The blanket module has therefore been modified and includes a slot with a width of 30 mm. The impact of the slot height on the neutron and photon fluxes is summarized in *Table 3* for three different slot heights. The narrowest slit has the smallest fluxes, though the fluxes through the 30 mm slot are still acceptable. The 30 mm slot has therefore been selected and is assumed for further thermal modelling.

First Mirror	Neutron Heating (W/kg)	Photon Heat (W/kg)	Total Heat (W/kg)
10 mm slot	4.45 (3.2 %)	54.9 (1.3 %)	59.4 (1.3 %)
30 mm slot	8.28 (4.1 %)	75.4 (2.0 %)	83.7 (2.0 %)
50 mm slot	13.6 (3.8 %)	100. (1.7 %)	114. (1.8 %)

Table 3 Neutron and photon heat loads on the first mirror for various slit heights

The neutrons and photons deposit energy in the plasma facing mirror. Since neutrons are absorbed by the mirror material, the fluxes decrease as a function of penetration depth. To enable more detailed heat deposition modelling, the mirror has been resolved in the penetration direction in three node points as shown in Figure 15. This first mirror has an assumed thickness of 80 mm which is larger than the mirror thickness currently foreseen (~10 mm). The first 20 mm will have the largest neutron and γ fluxes, and the last 40 mm the smallest. A small gradient of neutrons and γ's is found though even for mirrors of a thickness of 80 mm the heat deposition changes by less than 20%, suggesting that the mean free path of the neutrons is much larger than the mirror dimension (the γ's are generated and absorbed locally). The results are summarized in Table 4. The heat deposition due to neutrons and γ's can therefore be assumed as uniformly distributed over the mirror volume. One may note that γ heating is by far the larger contribution compared to neutron heating.

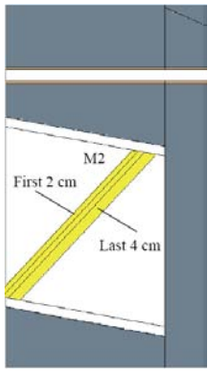

Figure *15* Mirror modelling with fine resolution for detailed heat deposition modelling

First Mirror	Neutron Heating (W/kg)	Photon Heat (W/kg)	Total Heat (W/kg)
0-20 mm	9.73	66.7	77.5
20-40 mm	8.79	63.0	72.0
40-80 mm	7.35	54.8	62.2

Table 4 Detailed heat deposition in the first mirror resolved in penetration depth

2.7.3 Thermo-Elastic Modelling

We assume plasma with 500 MW fusion power. The first mirrors facing the plasma are directly exposed to 14 MeV neutrons and secondary γ radiation from (n,γ) processes in the first mirror and elsewhere. The volumetric heating rates due to these were discussed in the previous section where it was found that the first mirror is exposed to a volumetric heating rate of 665 kW/m^3. Secondly, the mirror is exposed to direct irradiation from the plasma, originating mostly from bremsstrahlung (~40 MW), cyclotron radiation, and line radiation. Neutral particle fluxes constitute an additional heat load to be considered.

2.7.4 Plasma Steady-State Power Balance

The total heating power is composed of the fusion power and the auxiliary heating power. In steady state, this power must leave the plasma through the first wall and the divertor. We estimate the radiation and particle fluxes by a steady-state power balance in the plasma. We have:

$$\dot{H}_{in} = \dot{H}_{fusion} + \dot{H}_{auxiliary} = 500MW + 50MW = 550MW$$

$$\dot{H}_{out} = \dot{H}_{divertor} + \dot{H}_{firstwall}$$

$$\dot{H}_{firstwall} = \dot{H}_{neutrons} + \dot{H}_{radiation} + \dot{H}_{neutralparticles} + \dot{H}_{ions}$$

The first wall (and also the CTS first mirror) is being hit by radiation, neutral particles, charged particles, and neutrons. The 400 MW neutron power is accounted for by the

Monte Carlo simulations, leaving only 150 MW unaccounted for. As the distribution of these 150 MW between the first wall and the divertor is uncertain, this heat flux is treated parametrically. The radiation heat load depends for example on achievable impurity levels and the divertor heat load on the achievable confinement. It is assumed that the divertor heat load is at least 40 MW though it is designed for 100 – 150 MW [7]. This results in at most 110 MW on the first wall, giving 160 kW/ m^2 for a surface area of 680 m^2.

2.7.5 Mirror Steady-State Power Balance

Example geometries of first mirrors are illustrated in Figure 16 and Figure 17. The colour code refers to temperature distributions to be discussed below. The mirror is heated by neutrons and secondary gammas, radiation, and neutral particles from charge exchange processes. Few charged particles will reach the recessed first mirror. Cooling can occur by radiation cooling to the enclosure, conduction cooling through the thermal contact, and optionally an active cooling system if required. The power balance reads:

$$\dot{H}_{in} = \dot{H}_{neutrons} + \dot{H}_{radiation} + \dot{H}_{neutralparticle}$$

$$\dot{H}_{out} = \dot{H}_{radiationcooling} + \dot{H}_{conduction} + \dot{H}_{activecooling}$$

As mentioned above, the neutrons and gammas are accounted for resulting in a volumetric source term of 665 kW/m^3. The first mirror is partly protected by the blanket and the plasma is partially hidden. Irradiation from the plasma is therefore reduced by the view factor compared to the heat load on the first wall. As explained above, we assume at most 160 kW/m^2 on the first wall from the plasma in the form x-rays, UV radiation, and neutral particles. We then find a surface heat load of approximately 16 kW/m^2 on the first mirror with a view factor of 0.1. The view factor is estimated from the slit height and width and the distance from the mirror to the first wall (0.5 m x 0.03 m)/(0.2 m) $^2/\pi$. The curved mirror surface is assumed to have an angle of to 45° the propagation direction. The radiation from the plasma is supposed as diffuse. As this heat flux is uncertain, the parameter is scanned from 0-16 kW/m^2. The wavelength of the irradiation from the plasma is especially in the VUV, UV, and x-ray ranges. Irradiation at these wavelengths is mostly absorbed in the first few millimetres of the solid material [8], and it is therefore appropriate to model this radiation as a surface heat flux. It is assumed that this heat flux is fully absorbed (no reflection). Comparing the volumetric heating due to neutrons and γ's to the surface heating due to other plasma irradiation we find that the terms are of same magnitude. The surface heating is up to 500 W irrespective of mirror thickness, and the volume heating is about 20 W/mm mirror thickness (surface area of reflecting surface ~0.03 m^2, resulting in 200 W for a 10 mm thick mirror up to 600 W for a 30 mm thick mirror. As the first mirror is hotter than the enclosure supporting it, this heat flow can actually be regarded as beneficial radiation cooling which results in smaller active cooling demands on the mirror if these are required. The radiation heat transfer between the mirror and the enclosure is modelled with the Stefan-Boltzmann law assuming grey bodies with an emissivity of 0.5 and a surrounding wall temperature of 473 K for the baseline case. However, there is some scatter in the data of available values for emissivity [9]. Secondly, the detailed cooling system designed is currently being reviewed and the surrounding wall temperature is

therefore not accurately known yet. Due to these uncertainties, parameter sensitivity studies have been performed varying emissivity and the temperature of the surroundings.

A second heat sink is given by the support arm which sustains conduction heat flux to the cooled wall and constitutes a second inherent passive cooling system. The back side of the support arm is supposed to be actively cooled. Optionally, an active cooling system is considered. The active cooling system is assumed to be welded on the back side of the mirror, possibly facilitated by cooling channels. This backside cooling system is also compared to an internally cooled mirror with drilled cooling channels. The actively cooled surfaces are assumed to be at a temperature of 433 K. For the other surfaces the heat flux is given by the radiation heat exchange with the surroundings. The boundary conditions and source terms for the heat equation are summarized in Table 5 below. The temperature of actively cooled surfaces is varied parametrically as well.

Parameter	Baseline	Parameter range
Volumetric heating (neutrons and γ's)	665 kW/m^3	± 40%
Surface heating on plasma facing surfaces (UV and x-ray) (for normal angle of incidence)	16 kW/m^2	0 – 16 kW/m^2
Temperature of cooled surfaces	433 K	373 – 573 K
Temperature surroundings	473 K	423 – 623 K

Table 5 Baseline boundary conditions and source terms for the baseline case

2.7.6 First Mirror Material

In this study, the mirror material is assumed to be isotropic stainless steel (SS316). The material properties are taken from the ITER Material Properties Handbook [9] for a temperature of 200ºC summarized in Table 6. The material is assumed to be isotropic.

Density	7950 kg/m^3
Young's modulus (isotropic)	184 GPa
Poisson's ratio	0.3
Thermal expansion coefficient	16.9*10^{-6} 1/K
Thermal conductivity	15.7 W/(mK)
Heat capacity (not used)	520 J/(kgK)
Emissivity	0.5

Table 6 Assumed material properties of stainless steel at 473 K

As mentioned in Chapter 1, the possible choices of mirror material are plentiful, and will be the topic of a further study.

2.7.7 Numerical Methods

The heat equation and Navier's continuum equations have been solved in 3D by the finite element method (FEM). Radiation heat transfer with the surroundings is modelled as with the Stefan-Boltzmann law. The heat equation contains a source term accounting for the volumetric heating due to neutrons described above. Since the mirror deformation is small, the stress-strain problem can be decoupled from the temperature problem, facilitating a sequential solution. The partial integro-differential equations are discretized on irregular meshes composed of 10-node tetrahedral elements. Up to 500000 nodes were used to describe the system. The non-linear set of equations is solved iteratively with iterative solvers with the commercially available software ANSYS.

2.7.8 Uncertainties and Limitations

The discretization and iteration errors for the temperatures and the deformations are converged to an accuracy on the order of 0.1% which is far more accurate than limits imposed by uncertain boundary conditions (e.g. the fusion power for which we assume the nominal value of 500 MW) and material properties (e.g. emissivity). The volumetric heat source term is computed in the Monte-Carlo simulation to a convergence accuracy of 2%, though the model geometry is simplified, introducing additional modelling uncertainties. We model this heat source term as a constant over the mirror volume whereas it decreases slightly with penetration depth, giving an error of about 10% in the source term. As the direct plasma radiation depends for example on impurity levels and the particle flux on confinement, the surface heat load is not accurately known even for a nominal fusion plasma scenario and is therefore varied in a sensitivity study. Further modelling uncertainties stem from the estimation of the view factor, the angle of the surface, and the amount of reflected radiation from the plasma as well as for the heat exchange with the surrounding objects. The amount of reflected radiation depends on the frequency of the radiation and this has not been included in the modelling. The assumed temperature of actively cooled surfaces depends on the design of the cooling system, e.g. there can be non-uniformities in temperature. The governing equations contain also material properties which are assumed constant in the present study. Due to the strong non-linearity of the Stefan-Boltzmann law, the error is difficult to asses without parametric variations in this respect.

For the solution of the strain problem, we limit our study to thermal strains and defer strains due to electromagnetic forces to future studies. Uncertainties in the thermal strains then originate from the previously computed temperature gradients discussed above. Secondly, the base of the mirror support arm is assumed to have zero displacement, i.e. it is assumed fixed in space. This is of course not true as the entire structure changes temperature as well. This is irrelevant for computation of the von Mises stresses but is relevant for the computation of the absolute displacement of the mirror surface which redirects the beam. The material properties in Navier's continuum equations are also temperature dependent which has been neglected. Several topics mentioned above will be included in future modelling efforts.

2.7.9 Mirror Geometries

Figure 16 illustrates three initially conceived mirror shapes. Figure 16 a) and b) show the temperature distribution for this case for a 10 mm thick mirror in front view and back view, respectively. This mirror has external cooling channels to which cooling pipes can be welded. Figure 16c) and d) display the corresponding temperature distributions for a thicker mirror (20 mm) which also has external cooling channels. Figure 16 e) and f) picture an internally cooled mirror with drilled cooling channels. The temperature levels are large as a scenario with 50 kW/m^2 surface heat flux was assumed for these initial cases. This assumption was too strict as was shown in power balances in mirror and the reactor. The temperatures are largest on the irradiated surfaces, which are the reflecting mirror surface and the adjacent surface at

the upward edge which also has a line of sight to the plasma. The mirror design in this study has a support arm on the rear side, allowing for free thermal expansion. However, geometric constraints due to the enclosure hosting the mirror require that several edges are cut so as to fit the mirror into the small available space.

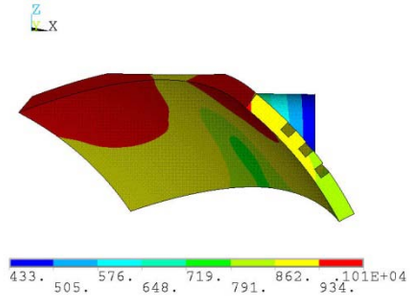

a) Front view, mirror thickness 10 mm, external cooling channels (6 mm), solid holder

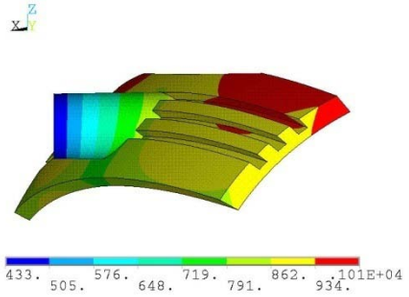

b) Back view, mirror thickness 10 mm, external cooling channels (6 mm)

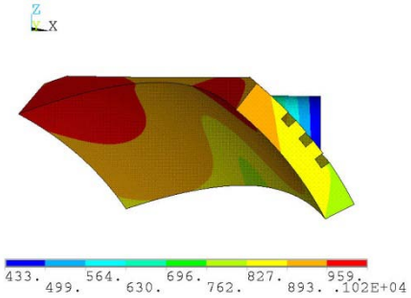

c) Front view, mirror thickness 20 mm, external cooling channels (6 mm)

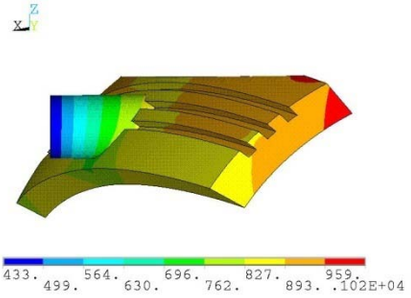

d) Back view, mirror thickness 20 mm, external cooling channels (6 mm)

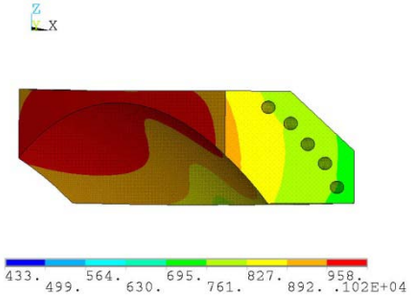

e) Front view, straight back mirror, internal cooling channels (6 mm)

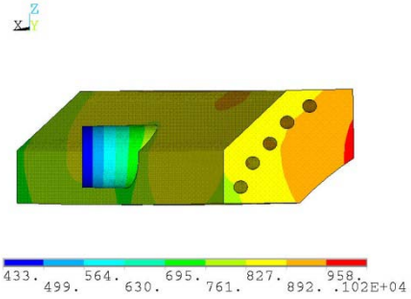

f) Back view, straight back mirror, internal cooling channels (6 mm)

Figure 16 Temperature distributions in Kelvin for 50kW/m2, loss of cooling scenario

While these mirrors are easy to manufacture, a few downsides are also noted: The temperatures are high especially on the corners. These corners do not reflect waves since the beam shape is elliptic. One can therefore cut off these corners. In this first design, a solid metal support arm was assumed which is disadvantageous as

discussed below. Additionally, the cooling channel cut-outs act as bottlenecks for conduction heat transfer and raise the temperature additionally since the smaller cross-sectional areas imply larger temperature gradients by Fourier's law. The cooling channels are therefore eliminated, the corners are rounded so as to satisfy an approximately constant safety margin with respect reflecting the elliptic beam, and the solid holder is replaced by a hollow holder. The current status of the first mirror design is displayed in Figure 17. As the geometry and boundary conditions are altered significantly, direct comparisons to Figure 16 may be misleading.

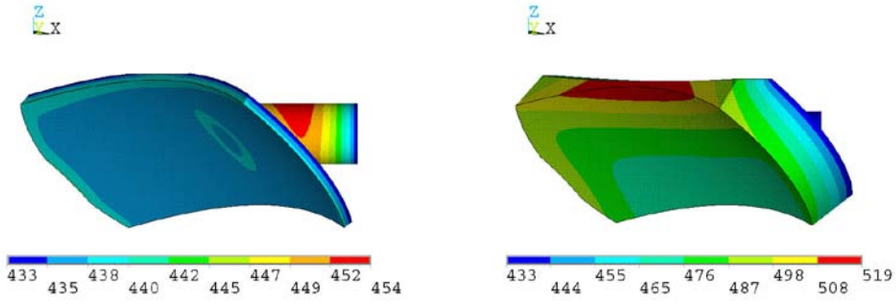

a) 5mm mirror b) 30 mm thickness

Figure 17 Temperature distributions in Kelvin for 16 kW/m2, active cooling scenario

2.7.10 Maximum Temperatures

As the heat load parameters are uncertain, they have been varied in large margins to estimate the sensitivity of the computed results to them. Figure 18 summarizes the results regarding the maximum temperatures for variations of several parameters and mirror thicknesses from 5 to 30 mm. Figure 18 a) describes the impact of surface heat load on the first mirror. The upper four curves with solid symbols reveal the maximum temperatures of first mirrors which are passively cooled by radiation and conduction alone. Obviously, the temperatures increase for larger surface heat fluxes. It can be noted that thicker mirrors have larger maximum temperatures than thin mirrors. The reason is that the characteristic penetration depth of neutrons in stainless steel (SS316) is much larger than the mirror thickness, implying that only a small part of the streaming neutrons is absorbed in the mirror and that the gamma and neutron heating power is proportional to the mirror volume (or the thickness) in this limit. Secondly, Fourier's law implies that heat flux from the reflecting surface to the back side of the mirror must be down a temperature gradient, which as well leads to larger temperatures for thicker mirrors. The lower four curves show the corresponding results for actively cooled mirrors, leading to the same conclusion. As the backside is cooled to 433 K, the maximum temperature is less sensitive to the plasma radiation heat load (though of course the active cooling demand increases with heat load). The thinner the mirror, the smaller the maximum temperatures and the temperature difference across the mirror thickness. Thin mirrors are clearly advantageous in this respect. However, the conclusion that thin mirrors are beneficial will have to be qualified since excessively thin mirrors are prone to thermal fingerprints of backside geometrical features. We select 16 kW/m2 as baseline for the other computations as it constitutes a worst case scenario.

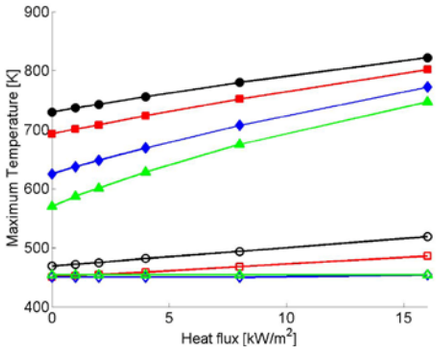

a) Maximum temperature vs. heat flux

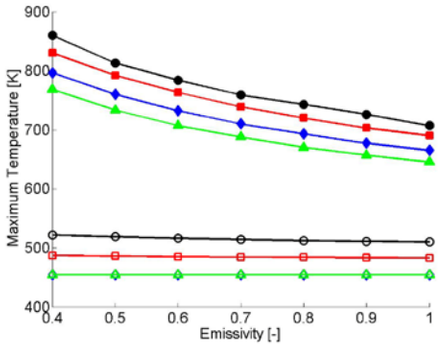

b) Maximum temperature vs. emissivity

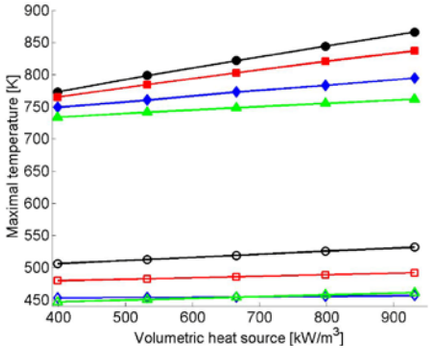

c) Maximum temperature vs. volumetric heat source

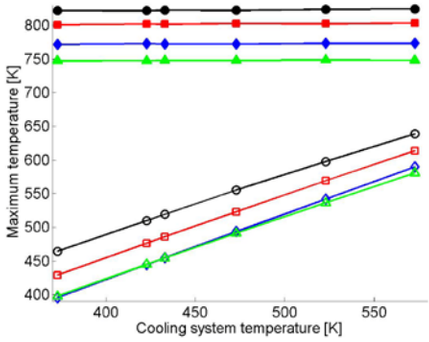

d) Maximum temperature vs. cooling system temperature

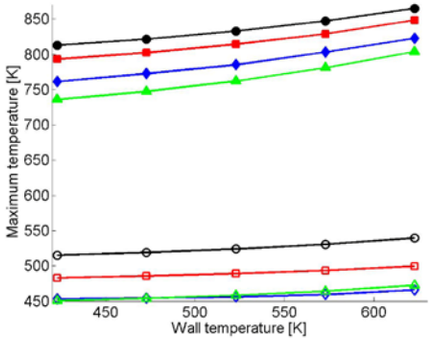

e) Maximum temperature vs. temperature of the surroundings

Figure 18 Maximum temperature as function of various parameters for various mirror thickness; Solid symbols: Radiation cooling, contoured symbols: Active cooling; ● -30mm, ■-20mm, ♦-10mm, ▲-5mm

The maximum temperature of the mirror is a function of material emissivity, especially for mirror cooling relying entirely on radiation and conduction. The sensitivity of the results to this parameter is addressed in Figure 18 b). The parametric variation of the emissivity must be carried out since there is considerable spread in the data due to dependence of the emissivity on for example surface roughness, temperature, or coating.

In fact, no code qualified values could be established yet reference [9]. The smaller the emissivity, the larger the temperature levels become, and large emissivities are therefore beneficial for the mirror option without active cooling. For actively cooled mirrors, the emissivity is unimportant since the active cooling contribution is much larger than the radiation cooling contribution. The emissivity of the baseline scenario is 0.5.

In Figure 18 c), the volumetric heat source term is varied up to 40% below and above the nominal value of 665kW/ m^3. The larger the volumetric heating, the larger the maximum temperatures become. The gradient is larger for thicker mirrors because the ratio of volumetric heat load to surface heat load increases with mirror thickness. The influence on the maximum temperature again becomes smaller for actively cooled mirror, though the cooling demand increases with volumetric heat load.

An overview of the impact of cooling system temperature is presented in Figure 18 d). For the mirrors without active cooling system on the backside, the influence of the cooling system temperature is marginal as only the temperature on the back of the support arm is varied, leading to flat curves in parametric variations. The maximum temperatures of mirrors relying on active cooling, on the other hand, rely strongly on the temperature of the cooling water which has not been defined yet. We assume 433K as nominal value for the temperature of actively cooled surfaces.

Also the temperature of the surroundings (the wall temperature of the enclosure supporting the mirror) has impacts on the maximum temperatures as Figure 18 e) demonstrates. Since the mirror has a direct line of sight to the plasma it is hotter than the surroundings, leading to cooling by radiation heat flux. This cooling effect decreases with increasing wall temperature of the surroundings for passively cooled mirrors though the effect is relatively small (heat flux is proportional to the difference of the temperatures to the fourth power). Radiation cooling is less important for actively cooled mirror which rely mostly on convection heat flux to the flowing water stream, leading to smaller gradients for actively cooled mirrors.

2.7.11 Maximum Displacements

As first estimate of the thermal deformation due to thermal strain, we use the maximum displacement vector magnitude which is defined for each point on the mirror surface between the burn condition and room temperature condition. This parameter is not sensitive to the direction of the displacement. The back of the holder is assumed to be fixed in x-direction while radial expansion of the holder is allowed. Figure 19 demonstrates that the maximum displacement magnitude is on the order of 1 to 2 mm for radiation cooled mirrors and 0.5 to 1 mm for actively cooled mirrors. The gradients of the curves are similar to those for the maximum temperature and are not discussed again. Generally, the thinner mirrors tend to be warped and displaced less than thicker mirrors. However, beam propagation modelling will be necessary to assess the impact of thermal deformation on the beam shape. The minimum displacement is found in the region where the mirror is mounted and the largest on the left side. The asymmetry arises due to the fact that the mirror is oriented at an angle in 3D space.

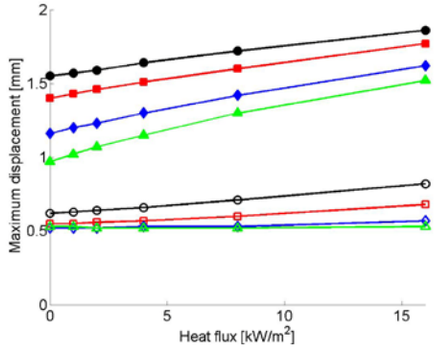

a) Maximum displacement vs heat flux

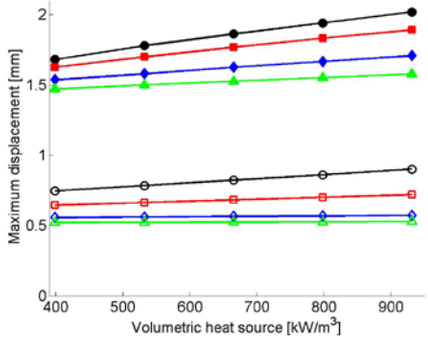

b) Maximum displacement vs volumetric heat source

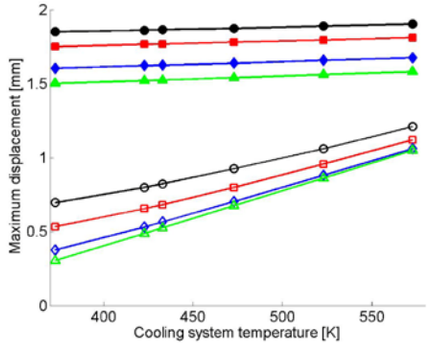

c) Maximum displacement vs cooling system temperature

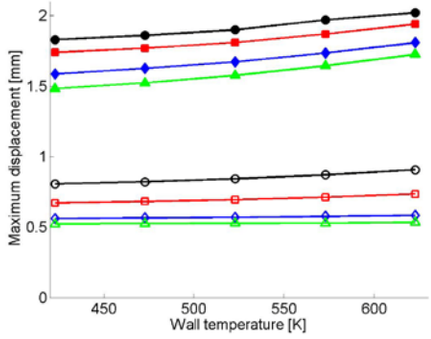

d) Maximum displacement vs temperature of the surroundings

Figure 19 Maximum displacement as function of various parameters for various mirror thickness; Solid symbols: Radiation cooling, contoured symbols: Active cooling; ● -30mm, ■-20mm, ♦-10mm, ▲-5mm

2.7.12 Maximum von Mises Stresses

Lastly, the impact of mirror thickness on thermal von Mises stresses is studied in Figure 20 for the parameter ranges of interest. Von Mises stresses give an indication of whether the stress is low enough to avoid the regime of plastic deformation. The von Mises failure hypothesis is applicable for ductile materials such as steel. The absolute levels can be changed by mirror design, but the impact of mirror thickness is clearly demonstrated: Thermal von Mises stresses increase with mirror thickness. Thinner mirrors will therefore have a larger safety margin against the regime of plastic deformation. Secondly, large thermal von Mises stresses can be remedied by active cooling. Ultimately, the first mirrors will have to be designed against electromagnetic forces which are not included in the present work. To reduce the stresses, large temperature gradients and sharp edges should be avoided at places where the stresses are high. Thin mirrors maintain low temperature gradients and are therefore advantageous. It will also be advantageous to distribute the cooling channels evenly over the back side if these are required. The modelling will be extended to assess the effect of rounding the edges in future work. Rounded corners will reduce the von Mises stresses considerably.

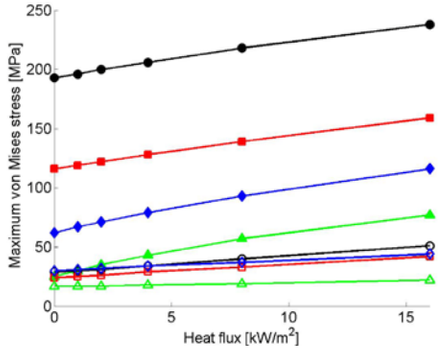

a) Maximum von Mises stress vs heat flux

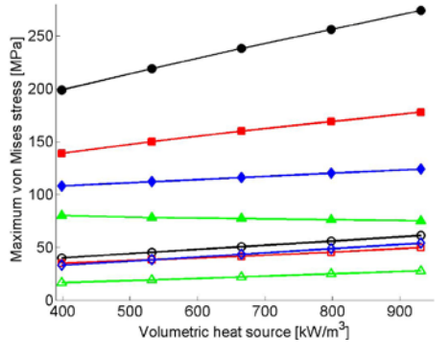

b) Maximum von Mises stress vs volumetric heat source

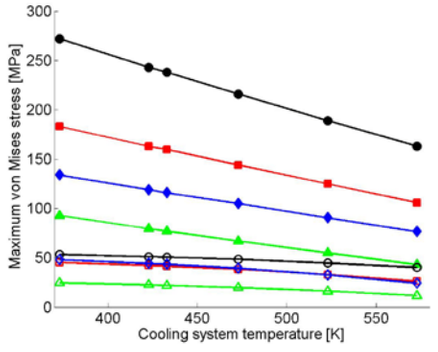

c) Maximum von Mises stress vs cooling system temperature

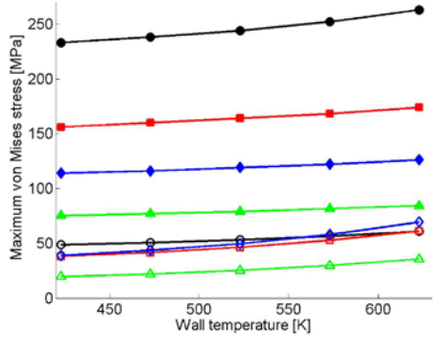

d) Maximum von Mises stress vs temperature of the surroundings

Figure 20 Maximum von Mises stress as function of various parameters for various mirror thickness; Solid symbols: Radiation cooling, contoured symbols: Active cooling; ●-30mm, ■-20mm, ♦-10mm, ▲-5mm

2.7.13 Massive versus Hollow Support Arm

Figure 21 shows the impact of the support arm geometry and cooling. Since bending resistance is mostly offered by the outer radii whereas the volumetric heating is uniform, the bending resistance per unit heating power is larger for outer radii (the second order area moment scales with the square of the distance to the central axis). One concludes therefore that hollow support arms are advantageous. However, it has been argued that the heat conduction loss through a massive holder may be much larger. The heat loss is proportional to the cross-section of the support arm which still leads to the conclusion that a hollow holder is preferable over a massive holder for the same cross-sectional area. Figure 21 demonstrates that the temperatures are comparable for massive and hollow holders, showing that the additional conduction heat loss is negligible or partly cancelled by the extra heat generation in the additional mirror material which now fills out the hole. The maximum displacement is also different only by several micrometers.

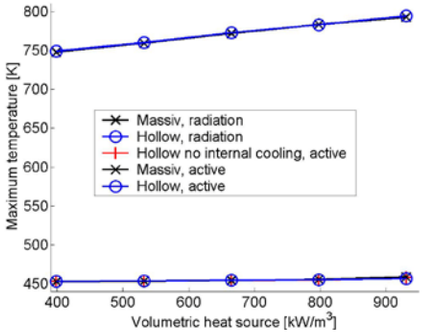

a) Maximum temperature

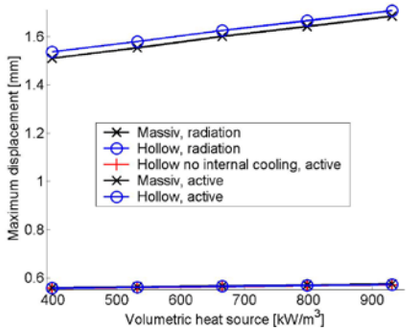

d) Maximum displacement

Figure 21 Massive vs. hollow support arm

2.7.14 Conclusions

The thermo-mechanical modelling suggests that thin mirrors are superior to comparable thick mirrors. It is recommended that unnecessary mirror corners be cut off such that the mirror geometry resembles the beam shape. A hollow mirror holder is preferred over a solid mirror holder. The mirror should be designed with as little material as possible. The modelling shows that neutron streaming should be blocked by a separate component if necessary. The mirror displacement has been found, showing that beam propagation modelling is necessary to assess the impact of thermal deformation. Future work will be dedicated to a detailed material selection, the characterization of propagation of the electromagnetic waves through the deformed quasi-optics, the effect of the horizontal gap between the blankets, cooling system design, and stress modelling accounting for rounded edges and electromagnetic forces.

3 Waveguide mounting on the inner vacuum wall

Optimize the size, materials and type of waveguide, and perform engineering designs of the waveguides, their mounting on the inner vacuum wall (taking into account the expected thermal expansion) and the connections to the antenna system. The design should consider the existing design analysis on related waveguide systems, such as the HFS reflectometer waveguides.

3.1 HFS waveguides feed-through the upper port duct

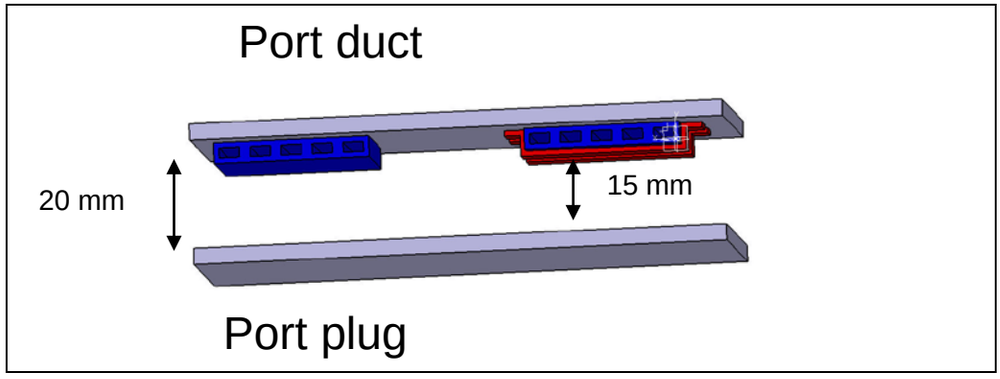

Figure 22: Fundamental waveguide mounted on the port duct

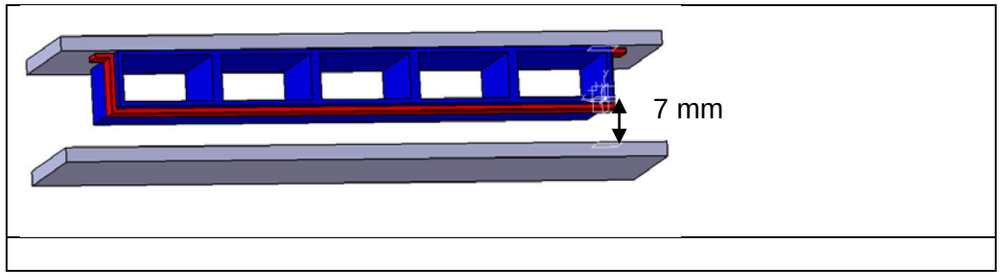

Figure 23: Overmoded waveguide mounted on the port duct

In Ref. [2] a conceptual design of the ITER CTS system was reported. An overview of the transmission line for the HFS CTS signal was presented. The HFS CTS signal is guided through 2 sets of waveguide arrays (shown in blue on Figure 22 and Figure 23), each containing 5 waveguides. The material should be copper or silver coated copper. The waveguides need to be mounted on the port duct by means of steel clamps marked with red colour on the figures. In Figure 22 a fundamental waveguide is used. The remaining distance between the clamp and the port plug is approximately 15 mm. The damping in fundamental waveguide for 60 GHz (WR15) is quite high (1.56 dB/m). With a total waveguide length on the order of several tens of meters (from the receiver antenna to the receiver electronics outside the torus hall) the total damping will not be acceptable. Using an overmoded waveguide with a

size of five times larger than the fundamental waveguide WR15 reduces the damping to 0.065 dB/m, but may give problems with excitation of higher order modes in bends. In this case the distance between port plug and clamp would be only 7 mm or less as shown in Figure 23. The horizontal width for an individual waveguide is 20 mm. These two options show the minimum and maximum space requirements.

4 Design study of the window assemblies

Perform a design study of the window assemblies needed for the large number of waveguides (both in the upper and equatorial ports), in particular in terms of required and available space. Take into account ongoing design studies on broadband (8–120 GHz) waveguide-feedthroughs for the reflectometer diagnostics.

Each of the systems of the collective Thomson scattering diagnostic on ITER is designed with the capability of measuring the fast ion distribution near parallel and near perpendicular to the magnetic field at different radial locations simultaneously. This implies multiple waveguides. Additional waveguides are also required for the proposed fuel ion ratio upgrade located in the same port of the LFS-BS system. The waveguides for the HFS-FS that run along the inner vacuum vessel wall are directed to the upper ports through cable feedthroughs to the port duct [2]. The waveguides for the LFS-BS located in the equatorial port are directed through the port plug back flange and bioshield. This poses a challenge to the available space needed for the vacuum interfaces for such a large number of waveguides using conventional flange design that require additional space. Design studies for the reflectometry diagnostic by the Kurchatov Institute [10][11] include the development a compact window assembly consisting of an in-line quartz window with fingers. The design is expected to have low reflections due to refractive index transition via the quartz fingers. Mock-up tests that include broadband range of frequencies (8-120GHz) are in progress.

5 Engineering design of the front-end quasi-optical components for the LFS system

Perform an engineering design of the front-end quasi-optical components for the LFS system in the port plug (including optional additions to the CTS system for fuel-ion-density diagnosis), addressing the location, size and mounting requirements (including cooling provision and requirements, thermal movement and alignment) of mirrors and receiver horns. Minimization of neutron streaming must be considered. The needs for high-power transmission lines and their assembly should also be defined. As described in the introduction, the boundary conditions on port-plug integration may or may not be established during the execution of this contract. If relevant, those conditions should be taken into account and their impact on performance assessed.

The probing beams for the HFS and LFS CTS parts are launched via the equatorial port #12 on ITER. The LFS CTS receiver is also located in the equatorial port #12.

5.1 The LFS launcher beam

The probing radiation for the LFS CTS system is provided from a gyrotron and fed by a corrugated waveguide into the equatorial port plug #12. The beam leaves the corrugated waveguide and propagates quasi-optically. The transition point is the red end of the depicted beam in Fig. 23. The beam characteristic is a circularly symmetric Gaussian beam. The required beam shape in the plasma has been calculated in the conceptual design [2]. In general, it is an anisotropic Gaussian beam. It is the blue end of the depicted beam in Fig. 23. In order to perform this transformation, two mirrors are required. The shapes of these two mirrors are calculated in Matlab (Figure 24).

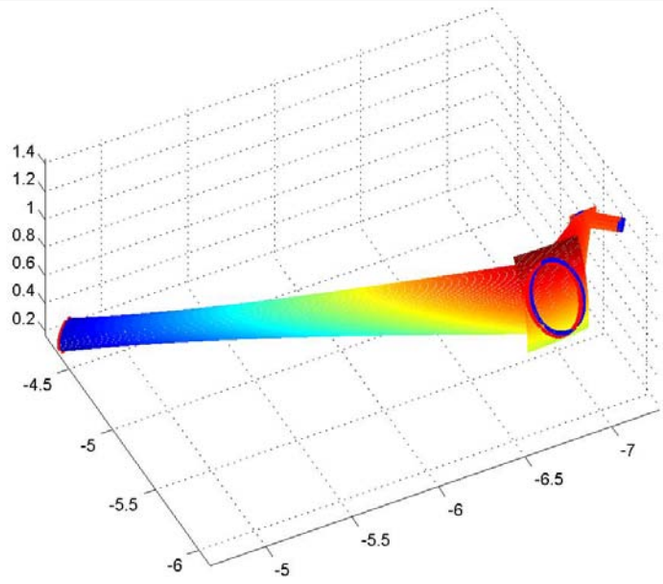

Figure 24: Calculation of the mirror surface required for the beam transformation

The Mirror shape is imported into CATIA V5, where the mirror design is performed. Figure 25 shows the mirror design and the beam pattern.

Figure 25: Mirrors and beam shape for the CTS LFS launcher beam

5.2 The LFS receiver

5.2.1 Two mirror solution

The backscattered CTS signal is captured with an antenna system in equatorial port #12. A quasi optical receiver antenna mirror, located behind a LFS blanket module transforms the beam (size approximately 400 mm in diameter) in a way that it can be accepted by a horn antenna. The desirable beam would be an isotropic beam, which can be detected by a circular horn antenna. In order to transform an in general astigmatic beam to an isotropic beam, two mirrors are required. The receiver mirror shapes are calculated in MATLAB and depicted in Figure 26 and Figure 27.

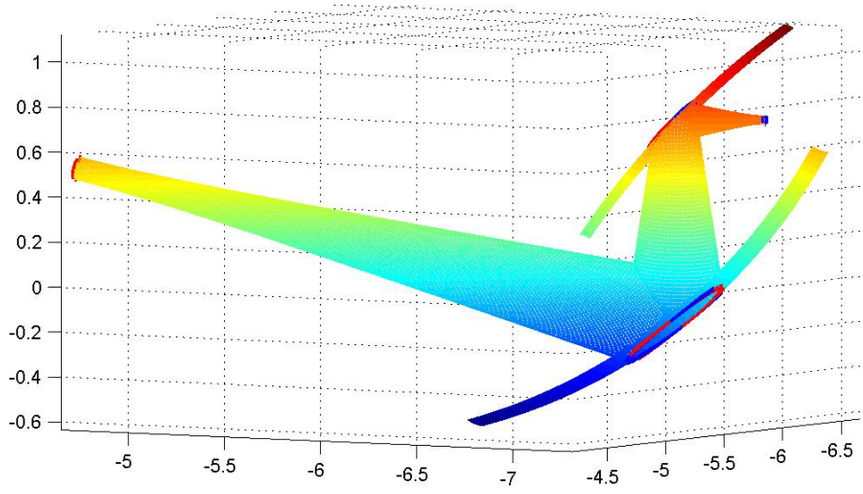

Figure 26: Modelling of the mirror shapes and the centre beam of the LFS CTS receiver

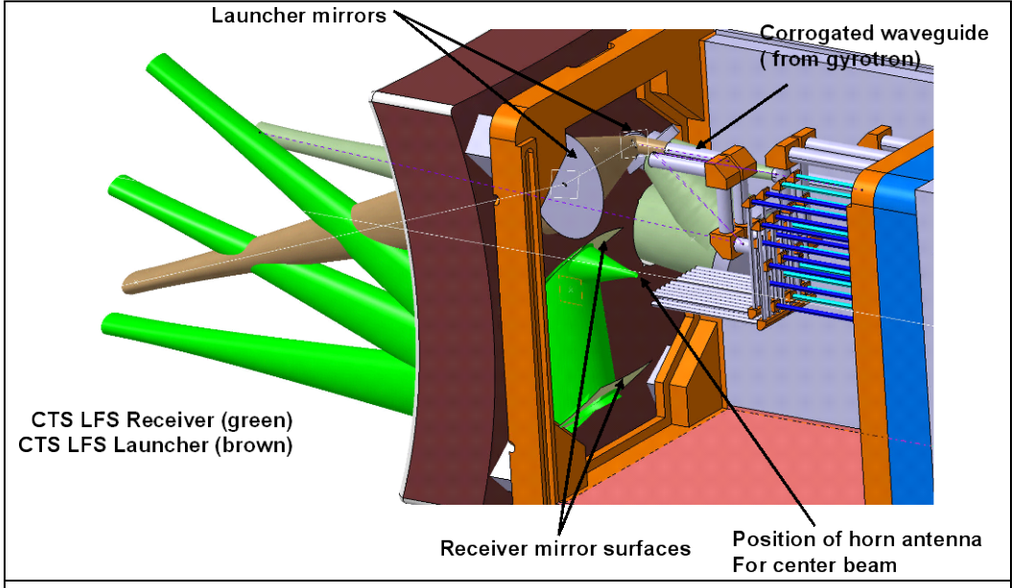

Figure 27: Equatorial port #12 on ITER with LFS CTS launcher and receiver beams, rear view

Scattered radiation from the different scattering volumes is captured using the same pair of mirrors. This leads to highly astigmatic beam for the beams from the extreme positions, which have an angle of +/- 15˚ with respect to the centre beam. The receiver beams are shown in green in Figure 27 and Figure 28. The beams from the extreme positions are only shown up to the first mirror.

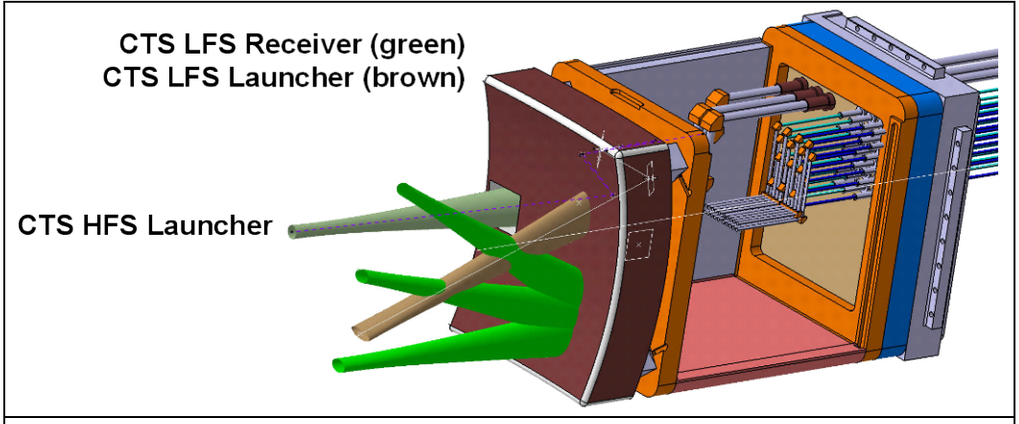

Figure 28: Equatorial port #12 on ITER with LFS CTS launcher and receiver beams, front view

5.2.2 One mirror solution

Due to the highly astigmatic beam pattern for the beams deviating from the centre beam, another approach is performed. This approach contains only one mirror. The disadvantage of this approach is the huge required mirror, the advantage is, that the beams, even for the extreme beams have at least so small dimensions inside the port, that there is no overlap between two neighbouring spatial channels. The possibility of horns, which can detect these beams still need to be investigated. Figure 29 shows a CATIA sketch of the mirror and the beam shapes.

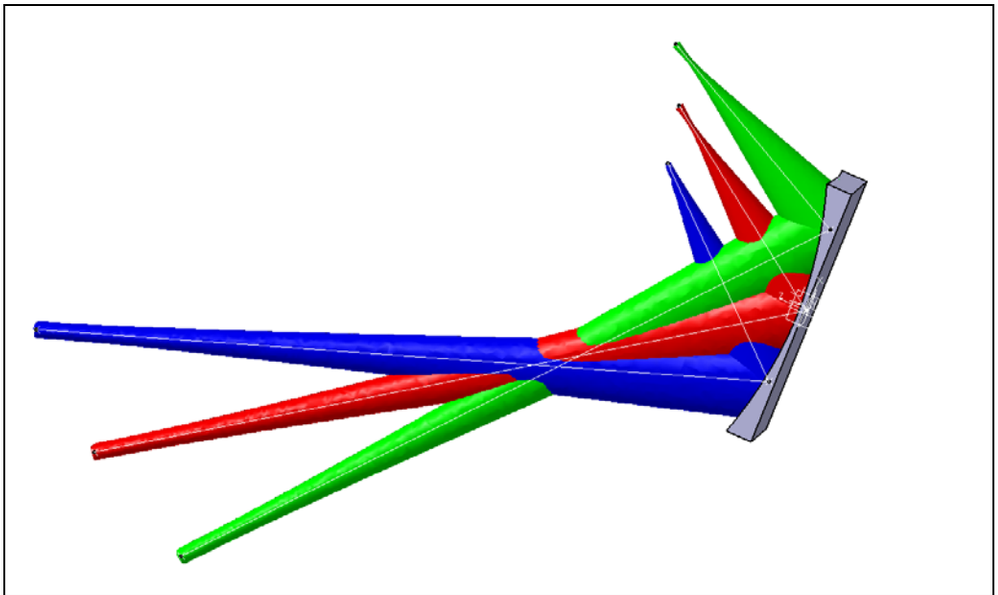

Figure 29: Sketch of the LFS receiver beams for a one mirror solution

6 Calibration methods

*Develop concepts and designs for calibration methods for both the HFS and the LFS systems.*The LFS receiver consists of one or two fixed quasi-optical mirrors that measure backscattered radiation and couples it to a distributed set of receiver horns. Each horn is located at a different distance from the mirror and collects scattered radiation from a different radial position in the plasma [2]. A more detailed description can be found in section 5.2. A calibration source should produce a known emission that covers the entire collection optics. Calibrating the front end is essential to monitor the changes in throughput from possible misalignments from thermal expansions and disruptions. A prototype of such a source is being developed for the ECE diagnostic on ITER [12]. The material of choice is silicon carbide (SiC) and tests are being carried out by the University of Texas group. Preliminary results of the source have shown flat temperature profile between 100 – 800 GHz [13]. However, the data is noisy for frequencies below 100 GHz due to the limitations of the Michelson measurements. A dialogue between the University of Texas group and Risø DTU has started to extend the tests down to 55 GHz.

As in the ECE diagnostic, the source will not be in direct line sight of the plasma, but will be located behind the blanket module. The first CTS mirror for the LFS-BS system is just behind the blanket module about 1 m distance from the blanket's plasma facing surface. Figure 30 shows the beam diameters (Gaussian radius × 3.2 = 96 % of the power) for different receiver beam as a function of distance from front-end mirror in the present design. Each beam dimension at the first mirror is about 450 mm in diameter.

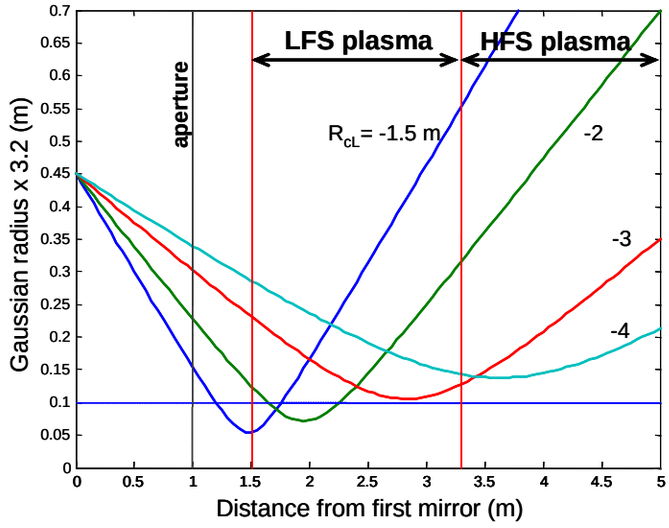

Figure 30 Beam diameters (Gaussian radius × 3.2) as a function of distance from front-end mirror. The curves are for different radii of curvature, Rcl, (in meters) at the mirror. The negative values of the radii of curvature indicate that the beams are focusing toward the plasma. The vertical red lines represent the position of the boundaries of different plasma regions. The vertical black line represents the position of the blanket aperture. The mirror size is 0.45 mm and the frequency of the Gaussian beam is 60 GHz.

Hence accommodating the calibration source will imply a larger distance between the plasma and the first mirror. The beam diameters for a first mirror displaced to 1.5 meters

from the blanket edge are displayed in Figure 31 for a beam diameter of 0.45 m (a) and 0.55 m (b) at the first mirror. The vertical beam dimensions at the scattering volume for the LFS system will have a direct impact on the CTS signal hence effect the diagnostic measurement requirement. Hence to reduce the vertical beam dimension in the plasma will require further enlarging the beams sizes at the first mirror. Figure 32 shows the most promising design for the LFS front end [see Sec. 5.2]. The figures shown in green are the dimensions required for full coverage of the source need to cover the optics. Hence displacing the entire optics about 0.5 m further away, would require increasing the mirror size by about 300 mm to 750 mm.

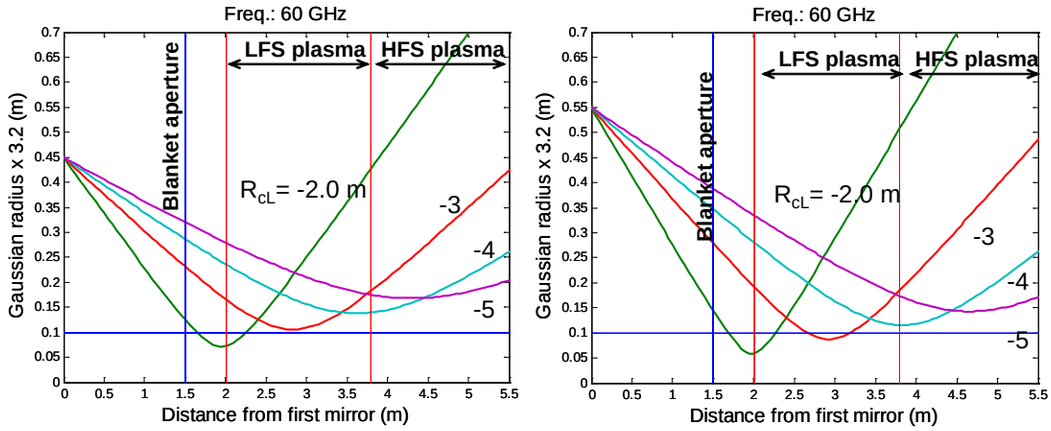

(a) (b)

Figure 31 Beam diameters (Gaussian radius × 3.2) as functions of distance from front-end mirror for the mirrors at 1.5 meters further inward.

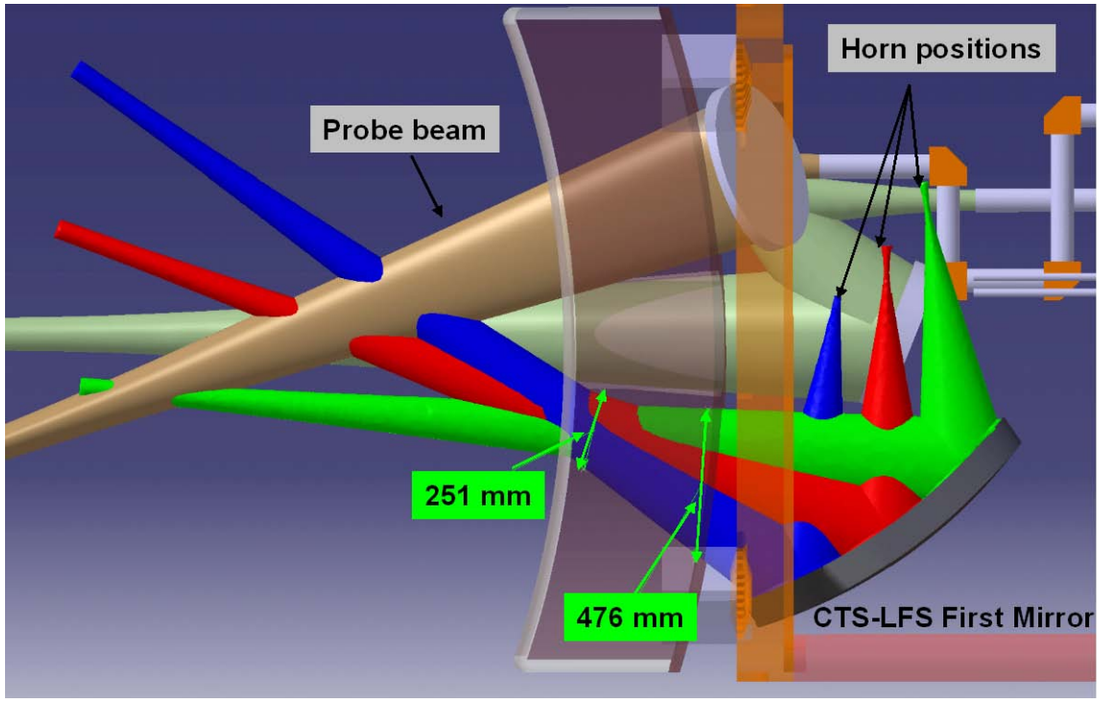

Figure 32. Side view of the CTS LFS front end installed in the equatorial port plug. The blanket module and the port plate are made semi transparent. The probe beam is in brown. Three of the ten receiver beams are shown by the blue, red and green those correspond to the upper most, middle and lower most extreme angle where their scattering volumes cover the entire LFS of the plasma.

7 Documentation

Assess existing documentation and assist the ITER IT in the updating of ITER documentation in this area.

Throughout the execution of this contract there have been consultations with the ITER IT. To facilitate the updating of ITER documentation this report will be provided to the ITER IT. The results in this report do not change any of the conclusions obtained in the feasibility study [1]. The design requirements presented in that section have not been changed. All design drawings in [2]-[4] have been further developed, but as described in the Outline plan in Section 1 several design and R&D tasks have still to be performed.

8 IPR

The Engineering design of the ITER Collective Thomson Scattering diagnostic described in this report is based on the feasibility study, the conceptual design, the report on detailed integrated design of the collective Thomson scattering (CTS) system for ITER, and the report on development of diagnostic components and techniques described and documented in the ref.: [1,2,3,4]. In addition to this, details in the design is performed utilizing the general knowledge of the individual authors of the report and on general known information found in textbooks, reports and other publications. The modelling work is based on commercial software.

The design is divided into the design of the HFS and the LFS antenna. The HFS receiver system consists of a mirror assembly and a receiver horn antenna. In order to verify the proper operation of the receiver system, which was modelled in Matlab and designed in CATIA, a full size mock-up of the HFS receiver antenna system and relevant parts of the involved blanket modules was produced. Design of the corrugated antenna horn for 60 GHz was based on general known information. A detector diode mounted on a translation stage and moving in two dimensions was used for measuring microwave beam pattern. The LFS antenna system is modelled using the same computer software.

The modelling of neutron and γ fluxes is being performed by Monte Carlo simulations with the MCNP-5 code [6], and thermo-elastic calculations of the first mirror of the HFS CTS system was performed using the commercially available software ANSYS.

The discussion on waveguide mounting on the inner vacuum wall, the design study of the window assemblies and the calibration methods was mainly based on some references to other work and simple design considerations.

Based on the description above we conclude that no particular background IPR was used in this contract. The results and this report are protected by intellectual property rights. The authors conclude that no further foreground IPR worth protecting has been generated under this contract.

Some of the work of this report was published in Ref. [14] and [15].

Acknowledgements

We would like to thank the ITER IT and EFDA staff for their useful help and comments particularly, Chris Walker, George Vayakis and Christian Ingesson.

References

[1] H. Bindslev, F. Meo, S. Korsholm, ITER Fast Ion Collective Thomson Scattering – Feasibility Study, part of the final report of EFDA Contract 01-654, (Association Euratom-Risø, Roskilde, Denmark)

[2] F. Meo, H. Bindslev, S. Korsholm, ITER Fast Ion Collective Thomson Scattering – Conceptual Design, part of the final report of EFDA Contract 01-654, (Association Euratom-Risø, Roskilde, Denmark)

[3] H. Bindslev, A.W. Larsen, F. Meo, P.K. Michelsen, S. Michelsen, A.H. Nielsen, S. Nimb, E. Tsakadze, Detailed integrated design of the collective Thomson scattering (CTS) system for ITER, EFDA Contract 04-1213 (Association Euratom-Risø, Roskilde, Denmark)

[4] S. Michelsen, H. Bindslev, S. Korsholm, F. Leipold, F. Meo, P.K. Michelsen, A.H. Nielsen, E. Tsakadze, Development of critical components and techniques for collective Thomson scattering, carried

out as deliverable 2 of TW6-TPDS-DIADEV (Association Euratom-Risø, Roskilde, Denmark)

[5] R. J. Wylde et. al., “Millimetre-wave Gaussian beam-mode optics and corrugated feed horns”, IEE proceedings, Vol. 131, Pt. H. No.4, August 1984

[6] Tech. Rep. LA-UR-03-1987, Los Alamos National Laboratory (2003).

[7] ITER Design Description Document G 17 DDD 6 R0.2 Divertor, 2004

[8] H-J Hartfuss, R Koenig and A. Werner, Plasma Phys. Control. Fusion 48 (2006) R83–R150

[9] ITER Material Properties Handbook (MPH), ITER Doc. G 74 MA 16 04-05-07 R0.1

[10] Design analysis for in-waveguide vacuum windows for ITER reflectometry, carried out as part of EFDA Contract 05-995 (Kurchatov Institute, Moscow, Russia)

[11] Design analysis for in-waveguide vacuum windows for ITER reflectometry, carried out under EFDA Contract 05-1318 (Association Euratom-ENEA, IFP-CNR Milano, Italy)

[12] M.E. Austin, P.E. Phillips, W.L. Rowan, R.F. Ellis, A.E. Hubbard, Review ITER ECE system; University of Texas

[13] P. E. Phillips, M. E. Austin, W. L. Rowan, 17th Topical conference on High Temperature Plasma Diagnostics, Albuquerque, New Mexico, May 11 – 15, 2008

[14] M. Salewski, F. Meo, H. Bindslev, V. Furtula, S. B. Korsholm, B. Lauritzen, F. Leipold, P. K. Michelsen, S. K. Nielsen, and E. Nonbøl, Review of Scientific Instruments,79, 10E729 (2008)

[15] F. Leipold, V. Furtula, M. Salewski, H. Bindslev, S.B. Korsholm, F. Meo, P. Michelsen, D. Moseev, S.K. Nielsen, M. S. Pedersen, Review of Scientific Instruments, vol: 80(9), Article no. 093501 (2009). American Institute of Physics

Risø DTU is the National Laboratory for Sustainable Energy. Our research focuses on development of energy technologies and systems with minimal effect on climate, and contributes to innovation, education and policy. Risø has large experimental facilities and interdisciplinary research environments, and includes the national centre for nuclear technologies.

Risø DTU
National Laboratory for Sustainable Energy
Technical University of Denmark

Frederiksborgvej 399
PO Box 49
DK-4000 Roskilde
Denmark
Phone +45 4677 4677
Fax +45 4677 5688

www.risoe.dtu.dk